

# Prospects For High Frequency Burst Searches Following Binary Neutron Star Coalescence With Advanced Gravitational Wave Detectors

J. Clark,<sup>1</sup> A. Bauswein,<sup>2</sup> L. Cadonati,<sup>1,3</sup> H.-T. Janka,<sup>4</sup> C. Pankow,<sup>5</sup> and N. Stergioulas<sup>2</sup>

<sup>1</sup>*University of Massachusetts Amherst, Amherst, MA 01003, USA*

<sup>2</sup>*Aristotle University of Thessaloniki*

<sup>3</sup>*Cardiff University, Cardiff, CF24 3AA, United Kingdom*

<sup>4</sup>*Max Planck Institute For Astrophysics*

<sup>5</sup>*University of Wisconsin–Milwaukee, Milwaukee, WI 53201, USA*

(Dated: June 23, 2014)

The equation of state plays a critical role in the physics of the merger of two neutron stars. Recent numerical simulations with microphysical equation of state suggest the outcome of such events depends on the mass of the neutron stars. For less massive systems, simulations favor the formation of a hypermassive, quasi-stable neutron star, whose oscillations produce a short, high frequency burst of gravitational radiation. Its dominant frequency content is tightly correlated with the radius of the neutron star, and its measurement can be used to constrain the supranuclear equation of state. In contrast, the merger of higher mass systems results in prompt gravitational collapse to a black hole. We have developed an algorithm which combines waveform reconstruction from a morphology-independent search for gravitational wave transients with Bayesian model selection, to discriminate between post-merger scenarios and accurately measure the dominant oscillation frequency. We demonstrate the efficacy of the method using a catalogue of simulated binary merger signals in data from LIGO and Virgo, and we discuss the prospects for this analysis in advanced ground-based gravitational wave detectors. From the waveforms considered in this work and assuming an optimally oriented source, we find that the post-merger neutron star signal may be detectable by this technique to  $\sim 10\text{--}25$  Mpc. We also find that we successfully discriminate between the post-merger scenarios with  $\sim 95\%$  accuracy and determine the dominant oscillation frequency of surviving post-merger neutron stars to within  $\sim 10$  Hz, averaged over all detected signals. This leads to an uncertainty in the estimated radius of a non-rotating  $1.6 M_{\odot}$  reference neutron star of  $\sim 100$  m.

PACS numbers: 04.80.Nn, 07.05.Kf, 97.60.Jd, 04.25.dk

## I. INTRODUCTION

The inspiral and merger of binary neutron star systems (BNS) is one of the most promising sources of gravitational waves (GWs) for the second generation of ground-based detectors, which include the US-based Advanced Laser Interferometer Gravitational Wave Observatory (aLIGO) [1], the French-Italian Advanced Virgo (AdV) observatory [2, 3] and the Japanese Kamioka Gravitational Wave Detector (KAGRA) observatory [4]. It is expected that the aLIGO-AdV network will reach design sensitivity in 2018-2020 [5], leading to the observation of 0.4–400 BNS coalescence events per year of operation [6], where the range in values are set by uncertainties on the BNS coalescence rate.

The internal composition and properties of matter at supranuclear densities is currently poorly understood and the equation of state (EoS) is not well constrained [7]. The GW signal from a BNS coalescence carries important information on the EoS and offers an unprecedented opportunity to probe the neutron star interior. As the stars grow closer, increasing tidal interactions imprint a distinctive EoS signature on the phase evolution of the GW waveform [8–10]. These tidal effects on the inspiral portion of the waveform may be detectable to distances  $\sim 100$  Mpc in aLIGO, leading to the determination of NS radii to an accuracy of about 1 km [11]. Complementary

and independent constraints on the EoS may be accessible from the post-merger part of the coalescence signal.

The most likely post-merger scenario is the formation of a massive ( $M > 2M_{\odot}$ ), differentially rotating neutron star, hereafter referred to as the post-merger neutron star (PMNS) [12–32]. The stability of the PMNS against gravitational collapse depends on its mass. Less massive systems result in a long-lived, stable PMNS. For more massive systems, or where insufficient material has been ejected during the merger, centrifugal and thermal effects result in a quasi-stable remnant which eventually undergoes gravitational collapse due to redistribution of energy and angular momentum via viscous processes, radiation of GWs and emission of neutrinos (“delayed collapse”). Sufficiently high-mass systems will result in prompt collapse to a black hole (BH), emitting a high-frequency ring-down GW signal at  $\sim 6\text{--}7$  kHz. The detection of these stellar-mass black hole ringdowns will be very challenging in the next generation of ground based GW detectors, due to their reduced sensitivity at high frequency; we will not consider them further in this discussion. We note that in [24] the authors suggest two subclasses of the delayed collapse scenario characterized by the lifetime of the post-merger remnant. In this work, however, we do not distinguish between the cases of long- and short-lived PMNS. Instead, we restrict our classification scheme to the two cases: i) prompt collapse to a BH and ii) PMNS formation. For simplicity, we will hereafter refer to (ii)

as ‘delayed collapse’. This term is also supposed to subsume cases which actually do not lead to a gravitational collapse at all because the PMNS is stable. Observationally, this scenario cannot be distinguished from a true delayed collapse by the GW signal immediately following the merger. Moreover, for some binary setups it may be very difficult to decide based on numerical simulations whether the resulting PMNS is stable or may eventually collapse because this would require long-term simulations which also take into account the relevant physics of the secular evolution of the PMNS. Such simulations are currently unavailable.

In case that the PMNS survives prompt-collapse, transient non-axisymmetric deformations in the post-merger remnant lead to a short duration ( $\sim 10$ – $100$  ms) burst of GWs which typically resembles an amplitude-modulated, damped sinusoid with a dominant oscillation frequency  $\sim 2$ – $4$  kHz associated with quadrupole oscillations in the fluid. In addition to the dominant oscillations, nonlinear couplings between certain oscillation modes have been identified, which appear as secondary peaks in the GW spectra [22]. The spectral properties of this signal carry a distinct signature of the EoS. In ref. [27], for example, the authors perform a large scale survey using a wide variety of different EoSs and establish the following correlation between the peak frequency  $f_{\text{peak}}$  of the post-merger signal from  $1.35$ – $1.35M_{\odot}$  binaries and the radius of a fiducial, non-rotating neutron star with mass  $1.6 M_{\odot}$ ,  $R_{1.6}$ :

$$f_{\text{peak}} = \begin{cases} -0.2823R_{1.6} + 6.284 & \text{for } f_{\text{peak}} < 2.8 \text{ kHz} \\ -0.4667R_{1.6} + 8.713 & \text{for } f_{\text{peak}} > 2.8 \text{ kHz,} \end{cases} \quad (1)$$

where radii are in km and frequencies in kHz. Allowing for an estimated uncertainty in the determination of  $f_{\text{peak}}$  and the maximum deviation from this correlation for the different EoSs considered in [27], it is possible that a single observation of the post-merger signal from a surviving PMNS could thus determine  $R_{1.6}$  to an accuracy of  $100$ – $200$  m. A relation between the dominant oscillation frequency and neutron star radii has been confirmed in [29], and an attempt to infer the neutron star compactness from a secondary peak is included in [31].

A single observation of the post-merger GW signal from delayed or prompt collapse can also constrain the threshold mass  $M_{\text{thresh}}$  for prompt collapse. In the case of a delayed collapse observation, the total mass measured from the inspiral signal provides a lower limit on  $M_{\text{thresh}}$ , and an upper limit can be inferred from the peak frequency  $f_{\text{peak}}$  and the fact that the frequency increases with the mass of the remnant [28]. In the case of unambiguous identification of a prompt collapse, the total mass measured from the inspiral signal represents an upper limit on  $M_{\text{thresh}}$ , leading to constraints on the maximum mass of a non-rotating star in isolation [28]. Similarly, recent work has demonstrated how two or more measurements of  $f_{\text{peak}}$  from systems with slightly different masses may allow the determination of the maximum

mass of cold, non-rotating neutron stars to within  $0.1 M_{\odot}$  and the corresponding radius to within a few percent [33].

Finally, with the projected Einstein Telescope [34] it may even be possible to use the post-merger signal to measure the rest-frame source mass and luminosity distance of a BNS system [35]. This measurement would break the mass-redshift degeneracy present in observations of the inspiral phase and permit the use of coalescing neutron stars as *standard sirens* with GW observations alone [36].

Most detectability estimates for these systems in the literature generally find that the post-merger signal may be detectable in aLIGO to distances of  $\sim$  few– $20$  Mpc, assuming an optimally oriented, overhead source and that an optimal signal-to-noise ratio (SNR) of  $\sim 5$  is sufficient for detection<sup>1</sup>. However, the post-merger signal has only recently begun to be described by analytical waveforms [29]. Consequently, to search for and characterize these signals, one must presently use more general morphology-independent search techniques. Here, transient bursts of GWs can be identified in the detector output data as excess power localized in the time-frequency domain (see e.g., [38–41]) and the impinging GW waveform can be reconstructed by considering the coherent signal energy coincident in multiple detectors [42–44] or by projecting the data onto bases formed from representative catalogues of simulations of the un-modelled signal [45, 46]. Additionally, in the case of the high-frequency GW burst following a binary neutron star coalescence, it is reasonable to assume that the time of coalescence will be known to high accuracy from the inspiral portion of the signal [47, 48], thus increasing the detection confidence for the post-merger part.

It is the goal of this work to determine realistic estimates for the detectability of the post-merger signal in the second generation of ground-based GW observatories using Coherent WaveBurst (CWB) [43], which is the algorithm used for unmodeled searches of gravitational wave transients [49, 50], and simulated BNS merger waveforms using a variety of EoSs. We also introduce a novel and computationally inexpensive algorithm for the analysis of the waveforms reconstructed by CWB which allows accurate determination of the outcome of the merger (delayed vs prompt collapse) and, where appropriate, a measurement of the dominant post-merger oscillation frequency.

This paper is structured as follows: in section II we describe the data analysis algorithm and model selection procedure proposed for the detection and characterisation of the post-merger GW signal; section III describes the experimental setup of the study, including a description of the LIGO data (§ III A) and the post-merger wave-

<sup>1</sup> We note that the simulations reported in [31] result in higher signal-to-noise ratios, increasing the detection horizon to  $20$ – $40$  Mpc, although these results do not seem compatible with those reported in [37].

form simulations (§ III B) used; in section IV we describe the results of our analysis in terms of the distance reach, expected detection rates and potential measurement accuracy using the algorithm proposed in this work. We conclude in section V with a discussion of our findings and future prospects.

## II. ANALYSIS ALGORITHM

In this section, we describe the algorithm used to detect, classify and infer the parameters of the putative post-merger signal, in two stages:

1. *Coherent Excess Power Detection*: we use the Coherent WaveBurst (CWB) algorithm [43] to detect statistically significant high frequency GW signal power in the data stream around the time of a known BNS coalescence. Once a signal is identified as significant with respect to the noise via a constrained likelihood statistic, the CWB algorithm reconstructs the detector responses using a coherent network analysis [42].
2. *Signal Classification and Characterization*: Spectral analysis of this reconstructed response from the first step is used to determine the outcome of the merger (delayed collapse and a surviving PMNS vs prompt collapse to a BH). If the outcome is identified as a surviving PMNS, the dominant post-merger frequency is recovered and used with equation 1 to determine the radius of a fiducial  $1.6M_{\odot}$  neutron star as in [27].

### A. Coherent WaveBurst

Searches for the inspiral GW signal from coalescing binaries are typically carried out using a matched-filtering technique and potentially large template banks [51–53]. The size and composition of these template banks is defined by the details of the targeted sources. While analytical expressions are available and appropriate for the inspiral portion of a BNS [54], phenomenological waveform families including the merger and ring-down are needed for higher mass binary black hole systems where the later part of the signal contributes significant SNR [55, 56]. These families, however, are not adequate for a post-merger search, since they do not yet include the effects of the neutron star matter on the orbital evolution during the inspiral, and they assume that the post-merger signal is the simple, quasi-normal mode ringdown expected from a Kerr black hole (e.g., [57]). While in the past, binary neutron star simulations were performed with a simple polytropic EoS and were focusing on the inspiral phase, most recent simulations are including microphysical EoS and also focus on the long-term post-merger evolution. However, the currently allowed sample of proposed EoS leads to a variety of different out-

comes. This motivates us to consider a hierarchical search approach, where the inspiral phase of the signal is detected via matched-filtering to post-Newtonian analytical waveforms and then followed-up using a morphology-independent analysis which identifies the post-merger signal.

The CWB algorithm is designed to identify and reconstruct generic transients in data collected from a network of interferometers. First, the data is decomposed into *pixelated* maps, where each pixel represents the localized energy of the data in a given time-frequency region. Clusters of time-frequency pixels across different interferometers’ maps are marked as having significant energy above the expected properties of the noise. Next, the analysis attempts to match the expected response of a passing gravitational wave — the two independent polarizations denoted  $h_+, h_{\times}$  — in the network with a maximum likelihood estimator:

$$\log L(h_+, h_{\times}) = \sum_{\Omega} 2\mathbf{x} \cdot \boldsymbol{\xi} - |\boldsymbol{\xi}|^2, \quad (2)$$

where the boldfaced symbols imply a vector quantity formed from each member of the network. The detector response  $\boldsymbol{\xi} = \mathbf{F}_+ h_+ + \mathbf{F}_{\times} h_{\times}$  represents the inferred signal in the data  $\mathbf{x}$ , such that  $\mathbf{x} = \mathbf{n} + \boldsymbol{\xi}$  and  $\mathbf{n}$  is the intrinsic interferometer noise. The dependence on source sky-location is encoded in the geometrical antenna patterns  $\mathbf{F}_+, \mathbf{F}_{\times}$ , defined in [58]. The two polarizations of the GW signal are free parameters in the likelihood statistic and  $\Omega$  is the event’s time-frequency area.

The likelihood for a time-frequency cluster is maximized over the source sky location and the waveform is reconstructed as:

$$h_+ = \frac{\mathbf{F}_+ \cdot \mathbf{x}}{|\mathbf{F}_+|^2} \quad (3)$$

$$h_{\times} = \frac{\mathbf{F}_{\times} \cdot \mathbf{x}}{|\mathbf{F}_{\times}|^2} \quad (4)$$

The likelihood is an optimal statistic under the assumption that the detector noise is stationary and Gaussian. In general, GW detectors can suffer from non-astronomical, environmental, mechanical, or electrically induced transients, referred to as *glitches*. To mitigate the effects of these glitches on the analysis and reject false positives, several statistics characterizing the consistency of the signal between interferometers, as well as additional likelihood constraints (e.g. imposing constraints on the polarization content of the signal) have been developed and applied in previous analyses [50, 59]. None of these additional constraints were utilized in this analysis as the detector data at high frequencies is dominated by photon shot noise and is far less contaminated by instrumental glitches than at lower frequencies.

Two statistics derived from the likelihood are used to identify and characterize potential GW events: the coherent network amplitude  $\eta$ , which is proportional to the

signal-to-noise ratio and is used to rank candidate events and establish their significance, and the network correlation coefficient  $cc$ , which is a measure of the degree of correlation between the detectors. Both statistics are described in detail in [60]. Small values of  $cc \ll 1$  are typical for uncorrelated background events, while true GW signals have  $cc$  close to unity. A threshold of  $cc = 0.5$  is used in the generation of CWB events in this analysis. Determination of event significance using  $\eta$  and the GW detection criterion is described in sec. III C.

### B. Post-merger Signal Classification & Characterization

A characteristic feature of the PMNS oscillation waveform is a distinct peak in the power spectrum around 2–4 kHz with a bandwidth of several tens of Hz. This is in addition to the roughly power-law decay across frequency from the late inspiral and merger, as well as one or more secondary oscillation peaks. An example of a typical PMNS waveform may be found in figure 1. On the other hand, in the prompt collapse scenario, one still expects power across these frequencies from the late inspiral and merger but any post-merger oscillation comes from the stellar-mass black hole ring-down at  $\gtrsim 6$  kHz. The waveform shown in figure 2 provides an example of the signal expected from prompt collapse.

These features in the GW signal spectrum may be identified in the waveforms reconstructed by the CWB algorithm, for candidate events that follow a detected low-mass binary inspiral. For this, we build an SNR-weighted average power spectral density (PSD) of the reconstructed waveform in a network of  $N_{\text{det}}$  detectors as:

$$P_i = \frac{1}{N_{\text{det}}} \sum_{j=1}^{N_{\text{det}}} \frac{\rho_j^{\text{rec}}}{\max_k(\rho_k^{\text{rec}})} P_{ij}, \quad (5)$$

where  $i$  indexes the frequency bins and  $\rho_j^{\text{rec}}$  is the SNR in the  $j$ -th detector. We model the PSD for the delayed collapse as the sum of a power law and a Gaussian:

$$S_{\text{NS}}(f) = A_0 \exp \left[ - \left( \frac{f - f'_{\text{peak}}}{2\sigma} \right)^2 \right] + A_1 \left( \frac{f}{f_{\text{low}}} \right)^\alpha, \quad (6)$$

where  $f'_{\text{peak}}$  is an estimator for the true peak frequency  $f_{\text{peak}}$  of the post-merger peak, and  $\sigma$  is its characteristic bandwidth.  $f_{\text{low}}$  is the lower bound on the frequencies analysed,  $\alpha$  is the power law for the decay component of the signal and the terms  $A_0$  and  $A_1$  set the amplitude scale of each component.

Since the post-merger signal is likely to be detectable only to  $\mathcal{O}(10)$  Mpc we assume that the inspiral portion for the signal is detected with high confidence (e.g.,  $\text{SNR} \sim 160$ , at design sensitivity [5]). Even at quite moderate SNRs (e.g.,  $\text{SNR} \sim 10$ ), the chirp mass

Total Mass [ $M_\odot$ ]	$f_{\text{peak}}^{\text{stiff}}$ [kHz]	$f_{\text{peak}}^{\text{min}}$ [kHz]
2.7 (1.35, 1.35)	2.15	1.75
3.2 (1.6, 1.6)	2.36	1.96
3.3 (1.65, 1.65)	2.40	2.00
3.8 (1.9, 1.9)	2.63	2.23

TABLE I. Estimates of the peak frequency of the post-merger GW signal for the stiffest EoS for the different masses considered in this analysis,  $f_{\text{peak}}^{\text{stiff}}$ . The analysis searches for spectral peaks above  $f_{\text{peak}}^{\text{min}}$ .

$\mathcal{M} = (m_1 m_2)^{3/5} (m_1 + m_2)^{-1/5}$  and symmetric mass ratio  $\eta = m_1 m_2 / (m_1 + m_2)^2$  can be measured from the inspiral signal, with fractional uncertainties as low as  $\Delta\mathcal{M}/\mathcal{M} \lesssim 0.1\%$  and  $\Delta\eta/\eta \sim 1\text{--}10\%$  [47, 61–66], which results in a total mass uncertainty of a few percent.

The total mass of the system sets a lower bound on the expected  $f_{\text{peak}}$ . Stars with a stiff equation of state are relatively under-dense resulting in a low  $f_{\text{peak}}$ . The  $f_{\text{peak}}$  for the stiffest equation of state (i.e., Shen) therefore represents a conservative lower limit on the probable value for a given mass configuration and unknown EoS. We probe frequencies up to 400 Hz below these values to account for uncertainty in the mass measurement and in the EoS. Lower bounds on the value of  $f_{\text{peak}}$  used for the different mass configurations are given in table I. Setting a lower frequency bound reduces the chance that the Gaussian component of equation 6 is fitted to secondary, lower frequency peaks in the reconstructed spectrum and significantly improves the robustness of the analysis. We place an *upper* bound on  $f_{\text{peak}}$  at 4 kHz; high enough to allow for the post-merger ringing from softer (i.e., high frequency) EoS, such as APR, and low enough that we expect no contribution from any black hole ringing, should the system undergo gravitational collapse.

In the case of prompt-collapse to a BH there will still be detectable signal power from the late inspiral and merger. Neglecting any contribution from the BH ring-down, which is at significantly higher frequencies, we model the reconstructed power spectrum as a power law,

$$S_{\text{BH}}(f) = A_1 \left( \frac{f}{f_{\text{low}}} \right)^\alpha, \quad (7)$$

where the terms are the same as those in equation 6.

We select between these two models for the reconstructed PSD using the Bayesian Information Criterion (BIC) [67], defined as:

$$\text{BIC} = -2 \ln \mathcal{L}_{\text{max}} + k \ln n, \quad (8)$$

where  $n$  is the number of spectral bins analysed,  $k$  is the number of free parameters in the model and  $\mathcal{L}_{\text{max}}$  is the maximum likelihood. The BIC arises from approximating the relative Bayesian posterior probabilities of models and provides a convenient measure of goodness-of-fit, weighted by the parsimony of the model. The model with the smallest value of the BIC is preferred. Assuming that



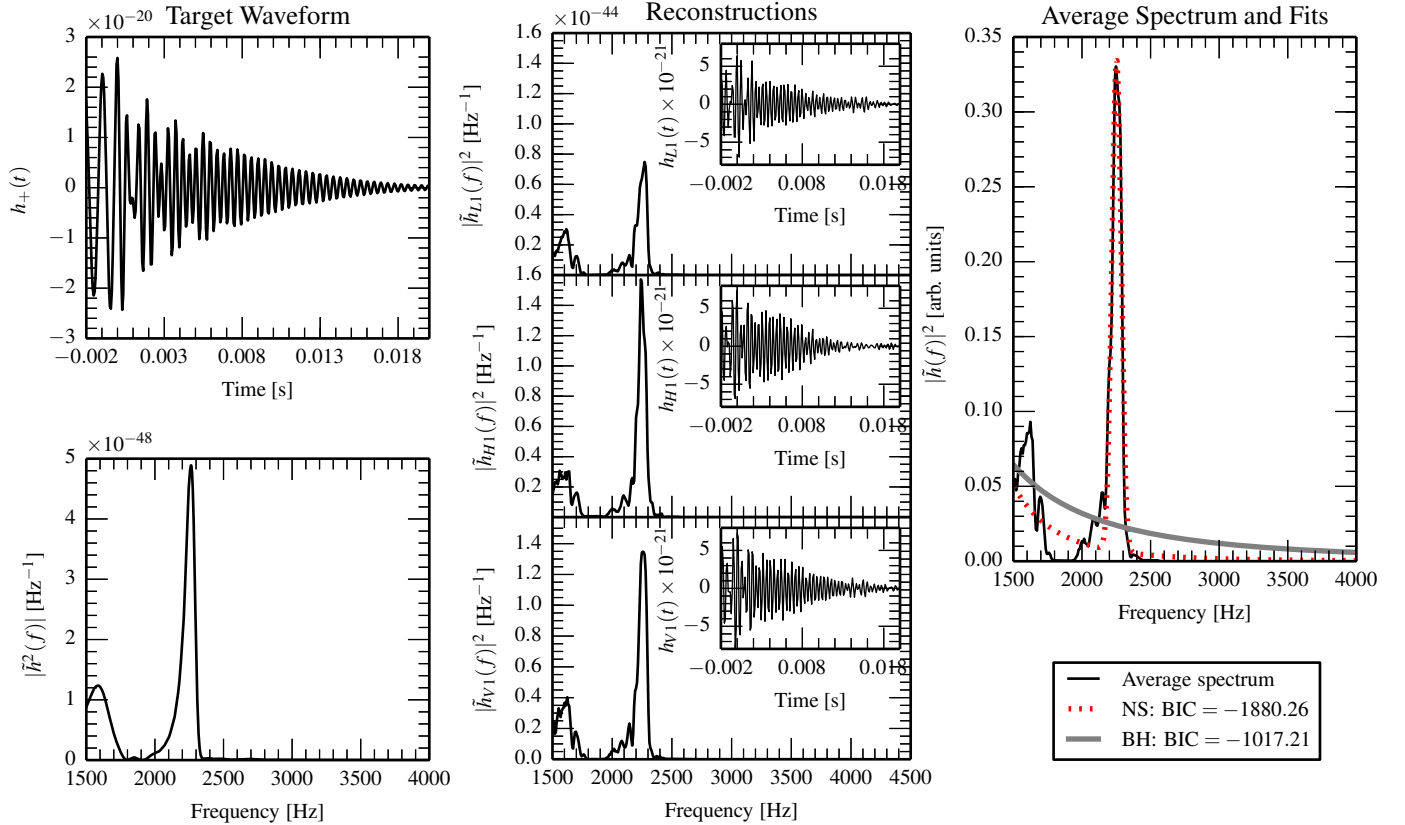


FIG. 1. Demonstration of signal characterization from the Shen EoS and  $1.35\text{--}1.35 M_{\odot}$  system, which results in a surviving PMNS. *Left column*: the time-series and power spectral density of the ‘plus’ (+) polarisation of the target waveform, for a source located 0.7 Mpc from the Earth. A small distance is deliberately chosen to provide a high SNR signal for demonstrative purposes. *Center column*: the power spectral densities and time series (insets) of the detector responses reconstructed by the CWB algorithm. The subscripts H1, L1 and V1 refer to simulated results from the LIGO detectors located in Hanford and Livingston, and the Virgo detector, respectively. *Right column*: the SNR-weighted average reconstructed power spectral density and fitted models. The model for the delayed collapse scenario is preferred in this instance, as indicated by the relative values of the Bayesian Information Criterion (BIC), defined by equation 8, for the delayed and prompt collapse scenarios.

the measurement errors are independent and identically distributed according to a normal distribution, the BIC is, up to an additive constant which is the same for all models:

$$\text{BIC} = n \ln \chi_{\min}^2 + k \ln n, \quad (9)$$

and

$$\chi_{\min}^2 = \frac{1}{n-1} \sum_{i=1}^n (P_i - S_i^*)^2, \quad (10)$$

where  $P_i$  and  $S_i^*$  are the average power spectral density of the reconstructed detector response and the value of the best-fitting model in the  $i^{\text{th}}$  frequency bin, respectively. The best-fit model is found via least-squares minimisation where the value of the center frequency of the Gaussian component  $f'_{\text{peak}}$  is constrained to lie above the relevant value from table I and the power law is constrained such that  $\alpha < 0$ .

Figure 3 shows the workflow of this detection and classification analysis pipeline. The proposed procedure is:

1. We assume a robust detection of an inspiral signal from BNS is achieved from a separate analysis, providing an estimate for the time of coalescence and total mass of the system.
2. A high-frequency CWB analysis is performed in a small time window around the time of coalescence of the BNS inspiral. The CWB analysis is constrained to [1.5, 4] kHz.
3. If CWB detects statistically significant excess power in a small time window around the time of BNS coalescence, assume this is associated with the coalescence and attempt to classify as follows.
4. Construct PSDs of detector reconstructions,  $\{P_i\}_j$  and average according to equation 5 to obtain  $\{P_i\}$ .

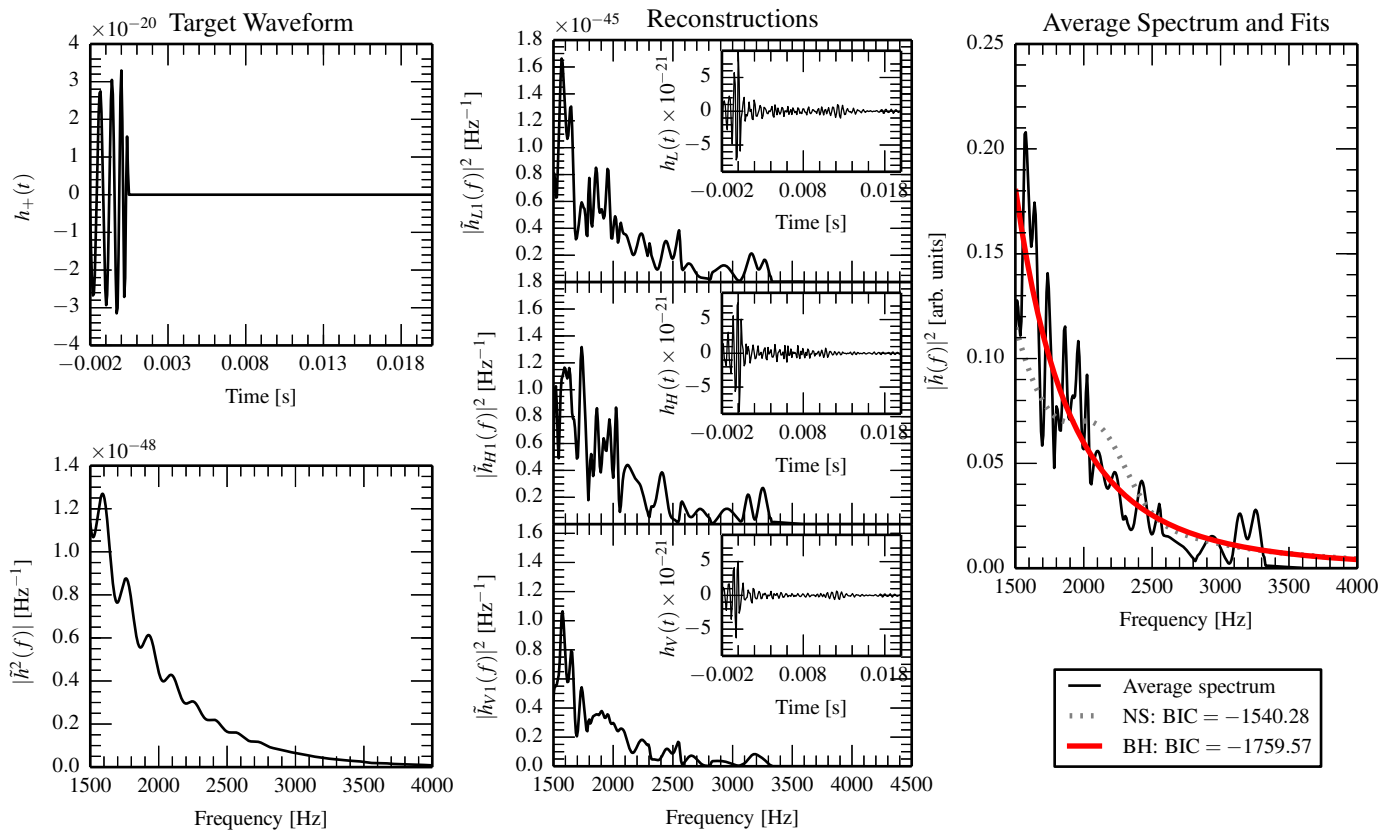


FIG. 2. Demonstration of signal characterization for the SFHo EoS and  $1.6\text{--}1.6 M_\odot$  system, which results in prompt collapse to a BH. BH quasi-normal ringing is not included in the numerical approach used here but lies at higher frequencies than are considered in this analysis. *Left column*: the time-series and power spectral density of the ‘plus’ (+) polarisation of the target waveform, for a source located 0.8 Mpc from the Earth. A small distance is deliberately chosen to provide a high SNR signal for demonstrative purposes. *Center column*: the power spectral densities and time series (insets) of the detector responses reconstructed by the CWB algorithm. The subscripts H1, L1 and V1 refer to simulated results from the LIGO detectors located in Hanford and Livingston, and the Virgo detector, respectively. *Right column*: the SNR-weighted average reconstructed power spectral density and fitted models. The model for the delayed collapse scenario is preferred in this instance, as indicated by the relative values of the BIC for the delayed and prompt collapse scenarios.

5. Fit models described by equations 6, 7 to  $\{P_i\}$  and compute  $\Delta\text{BIC} = \text{BIC}_{\text{BH}} - \text{BIC}_{\text{NS}}$ .
6. If  $\Delta\text{BIC} > 0$ , the PMNS model is preferred and the best-fitting value of  $f'_{\text{peak}}$  provides our estimate of the peak frequency of the post-merger oscillations.

### III. EXPERIMENTAL SETUP

The efficacy of the method outlined in section II is determined via Monte Carlo simulations in which simulated post-merger signals are superimposed on realistic detector data. In this section, we describe the data and waveform simulations used.

#### A. GW Detector Data

Data acquired by aLIGO and AdV is unlikely to be Gaussian or stationary and it is helpful to demonstrate that our analysis method is robust to such features by analysing realistic detector data. To do so, we use a week of data recorded by the initial generation instruments in 2007, recolored to the advanced detector design sensitivities, following the procedure in [68].

The LIGO data is recolored to have the Advanced LIGO design sensitivity given by the zero-detuned, high-power noise curve [69], while the Virgo data is recolored to have the Advanced Virgo design sensitivity, given by the dual recycled, 125 W, tuned signal recycling configuration [70]. This choice of detectors and noise curves loosely corresponds to a plausible GW detector network configuration for c.2020 [5]. Figure 4 shows the noise amplitude spectral densities (ASD) of the recolored data

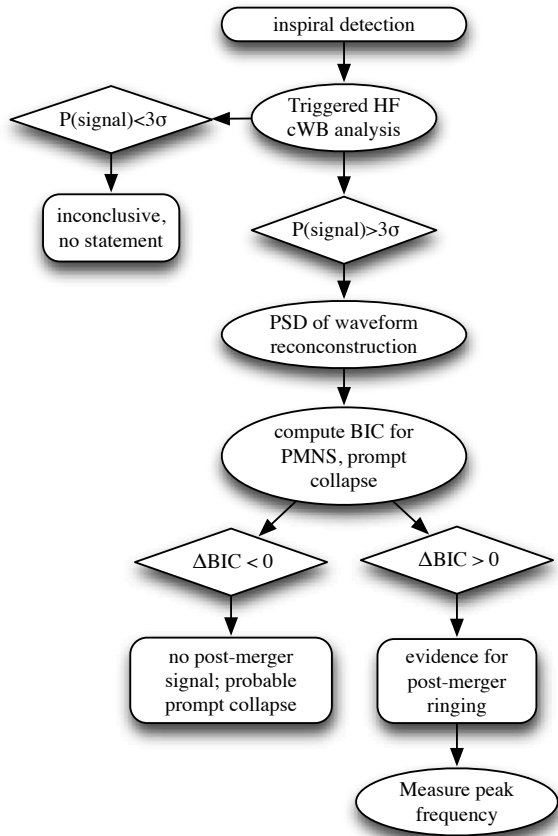


FIG. 3. Proposed data analysis pipeline for the detection and characterization of high-frequency GW signals following binary neutron star coalescence. The CWB un-modelled analysis algorithm is used to detect and reconstruct a high-frequency component to the GW signal temporally coincident with the inspiral signal from BNS coalescence. The Bayesian Information Criterion (BIC) is then used to select between models for the frequency content for the post-merger signals to determine whether the outcome of the BNS merger was prompt collapse to a black hole or the formation of a post-merger neutron star remnant.

for each detector, where the colored regions indicate the variation between the 5<sup>th</sup> and 95<sup>th</sup> percentiles of the ASDs, measured over the analysed data.

The data from this period is not contiguous; the detectors were not always operational and environmental artifacts and instrumental glitches affect the quality of the data. Such times are identified and removed from the analysis following the procedures described in [60, 71, 72], leaving a total analysed time of 3.87 days.

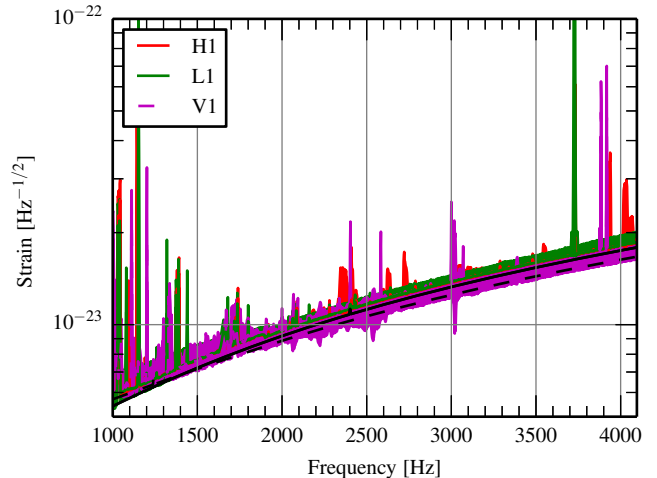


FIG. 4. The noise amplitude spectral density of the recorded data from the LIGO (H1, L1) and Virgo (V1) detectors used in this analysis. Shaded regions (color online) indicate the 5<sup>th</sup> (lower edge) and 95<sup>th</sup> (upper edge) percentiles of the variation in the noise floor for the data used. Black solid (dashed) curves indicate the design sensitivities of the aLIGO (AdVirgo) detectors used for this study [69, 70].

## B. Binary Neutron Star Coalescence Simulations

### 1. Merger Simulations

The waveforms used in our analysis are extracted from hydrodynamical simulations. These calculations are performed with a relativistic smooth particle hydrodynamics code, which employs the conformal flatness approximation for the solution of the Einstein field equations [73, 74]. Details on the numerical model can be found in [16, 27, 75, 76]. A comparison to fully relativistic grid-based simulations has revealed a quantitatively very good agreement [27, 29, 31]. In comparison to [27] we implemented an improved version of the artificial viscosity scheme (see [16, 77]) which reduces the artificial viscosity in dominantly rotational flows and causes less numerical damping of the fluid oscillations in the postmerger phase. The oscillation frequencies remain basically unchanged compared to the results presented in [27], while the artificial damping of the GW amplitude is reduced.

The prime goal of this study is the extraction of equation-of-state properties from the gravitational-wave detection of the neutron-star coalescence postmerger phase. Since the properties of high-density matter are only incompletely known, the numerical modeling relies on different theoretical descriptions of the equation of state (see e.g. [78] for a review). For this work we employ a large variety of microphysical EoS models to ensure that the full range of possible signatures is covered (see Tab. II). All equations of state are compatible with the current lower limit on the maximum mass of nonrotating

TABLE II. The nuclear equations of state used in this study. References are provided in the first column. Equations of state indicated by “approx” refer to models which rely on an approximate treatment of thermal effects, whereas “full” marks equations of state which provide the full temperature dependence.  $M_{\max}$ ,  $R_{\max}$ , and  $\rho_c$  are the gravitational mass, circumferential radius, and central energy density of the maximum-mass Tolman-Oppenheimer-Volkoff configurations. We list  $\rho_c$  in units of the nuclear saturation density  $\rho_0 = 2.7 \times 10^{14}$  g/cm<sup>3</sup>.  $R_{1.35}$  and  $R_{1.6}$  are the circumferential radii of 1.35 and 1.6  $M_{\odot}$  neutron stars.

EoS	$M_{\max}$ [ $M_{\odot}$ ]	$R_{\max}$ [km]	$R_{1.35}$ [km]	$R_{1.6}$ [km]	$\rho_c/\rho_0$
APR [81] (approx)	2.19	9.90	11.33	11.25	10.4
NL3 [82, 83] (full)	2.79	13.43	14.75	14.81	5.6
DD2 [83, 84] (full)	2.42	11.90	13.21	13.26	7.2
Shen [85] (full)	2.22	13.12	14.56	14.46	6.7
TM1 [86, 87] (full)	2.21	12.57	14.49	14.36	6.7
SFHx [88] (full)	2.13	10.76	11.98	11.98	8.9
SFHO [88] (full)	2.06	10.32	11.92	11.76	9.8
TMA [87, 89] (full)	2.02	12.09	13.86	13.73	7.2

neutron stars of about 2  $M_{\odot}$  [79, 80]. The considered equations of state yield maximum gravitational masses of nonrotating neutron stars from 2.02 to 2.79  $M_{\odot}$ . Neutron star radii vary between 11.33 km and 14.75 km for 1.35  $M_{\odot}$  neutron stars and thus cover a significant part of the range of typical radii constructed with various allowed EoS. Details on the stellar properties for the specific models can be found in Tab. II and in [27, 33], which provide also the mass-radius relations. All except for one equation of state (APR) take into account the dependence on temperature and composition (electron/proton fraction). For the APR model, which provides only the zero-temperature behavior, we employ an approximate description of thermal effects (see e.g. [76], which discusses also the reliability of the approximate treatment).

The merger simulations start from quasi-equilibrium orbits a few revolutions before the coalescence. Initially, the temperature of the neutron stars is set to zero and the electron fraction is determined by neutrinoless beta-equilibrium. The intrinsic spin of neutron stars is assumed to be small compared to the orbital motion because the viscosity of neutron-star matter is not sufficient to yield tidally locked systems during the inspiral [90, 91]. Hence, we adopt an irrotational velocity profile (see [30] for an inclusion of spins in the case of an ideal gas equation of state).

Binary neutron star observations suggest (in accordance with population synthesis studies) that symmetric systems with two stars of about  $\sim 1.35 M_{\odot}$  dominate the binary population [78, 92]. Therefore, the majority of waveforms used in this study are extracted from merger simulations of equal-mass binaries with a total mass of 2.7  $M_{\odot}$ , but we also explore cases with higher masses. It

is worth noting that similar relations between the dominant GW oscillation frequency and fiducial neutron star radii exist also for other binary masses [93]. We leave the investigation of unequal-mass systems for the future, but note that the dominant oscillation frequency of the postmerger remnant resulting from asymmetric binaries is very close to the one from a symmetric merger of the same total mass (e.g. [27, 29]).

For most investigated binary setups the merging results in the formation of a hot, massive, differentially rotating neutron star. The rapid differential rotation and thermal pressure support stabilize the remnant also in cases when the total binary mass exceeds the maximum mass of static non-rotating neutron stars. The collision induces strong oscillations, in particular, the quadrupolar fluid mode is strongly excited and generates the pronounced peak in the gravitational-wave spectrum (Fig. 1) (see [22] for the identification of several oscillation modes in the merger remnant). After angular momentum redistribution and the extraction of energy and angular momentum by gravitational waves, the remnant possibly collapses to a black hole on a longer time, which typically exceeds the simulation time of about 20 ms after merging. The exact collapse time scale depends strongly on the total mass and also on other (partially not modelled) dissipative processes like magnetic fields, neutrino cooling and mass loss.

For sufficiently high total binary masses the remnant cannot be supported against the gravitational collapse and the merging leads to the direct formation of a black hole on a dynamical time scale. In our set of models the SFHO with 3.2  $M_{\odot}$  total binary mass represents such a case (see waveform in Fig. 2). Note that our numerical approach does not allow to simulate the quasi-normal ringing of the BH. The oscillations of the BH occur at higher frequency than the [1.5, 4.0] kHz interval considered in this analysis and at smaller amplitude and, therefore, are unlikely to be confused with the signature of the NS postmerger remnants [94]. The threshold binary mass which results in the prompt collapse has been found to depend in a particular way on the equation of state and may yield information on the maximum mass of non-rotating neutron stars [28]. Therefore, we are also interested in distinguishing observationally the prompt collapse and the formation of a neutron star remnant. Note that the DD2 model with 3.2  $M_{\odot}$  total binary mass and the NL3 simulation with 3.8  $M_{\odot}$  total binary mass constitute models which are “close” to the prompt collapse because their binary masses are approximately 0.1  $M_{\odot}$  below the threshold. For both calculations the collapse still did not occur until the end of the simulation.

## 2. Hybrid waveforms

The finite simulation time and the numerical damping of the postmerger oscillations imply an underestimation of the actual GW amplitude. In an attempt to ac-



commemorate this shortcoming of our approach we also include a set of hybrid waveforms, constructed from a subset of the numerical waveforms described in the previous section. We extend the numerical waveform with an analytically prescribed waveform. The analytical part is described with a sinusoidal waveform, which follows a prescribed frequency evolution and damping behavior. The analytical model waveform is attached to the numerical waveform when the numerical amplitude has decayed to one half of the initial postmerger GW amplitude. This happens after several milliseconds when the remnant enters a quasi-stationary phase. The initial frequency of the analytical waveform is chosen to be the frequency of the GW signal at the matching point. We make conservative assumptions about the further evolution of the frequency and the damping timescale of the analytical model as explained below.

The damping of the postmerger oscillations and the evolution of the dominant oscillation frequency may be affected by different physical processes, such as gravitational wave emission, magnetic fields, neutrino heating and bulk viscosity (e.g. [95–97] and references therein). Here, we assume that the extraction of energy and angular momentum by gravitational waves is the dominant process responsible for the damping. Currently, there are no reliable estimates of the timescales of the other damping mechanisms, which is why we restrict ourselves to pure GW damping.

For cold, nonrotating NSs the damping timescale of the fundamental quadrupolar fluid mode is known to depend on the star’s mass and radius (see, e.g. [98]). However, the postmerger remnant is a hypermassive object rotating rapidly with strong differential rotation. For such a case, there still exists no calculation of the actual damping timescales (see [99] for the status on the subject).

The damping timescales due to gravitational wave emission, assuming a quasi-stationary background, will be affected by a number of factors: a) rapid rotation, b) differential rotation, c) high mass, d) the equation of state, e) strong field gravity. In addition, if the background is evolving on a comparable timescale, then this will result in a time-dependent damping timescale. In the absence of a proper calculation that takes all of the above effects into account simultaneously, we are forced, at this point, to resort to some approximations in order to estimate upper and lower bounds for the expected damping timescale for each particular merger event we consider. Next, we give a detailed account of how we arrive at the particular upper and lower bounds used in the present work. We focus on the *corotating*  $l = m = 2$   $f$ -mode, as this is the oscillation mode that is more likely to be excited during the merger of two neutron stars with a frequency of  $\sim 2 - 3$  kHz. The corresponding counter-rotating mode will likely have a lower frequency in the inertial frame, as it is dragged towards corotation by rotation.

As an estimate for an *upper bound* on the damping

timescale, we apply the empirical formula from [98]:

$$\frac{1}{\tau_0[\text{s}]} = \frac{\bar{M}^3}{\bar{R}^4} \left[ 22.85 - 14.65 \frac{\bar{M}}{\bar{R}} \right], \quad (11)$$

where  $\tau_0$  is the damping timescale (in seconds) of an  $l = 2$   $f$ -mode of a star of dimensionless mass  $\bar{M} = M/1.4 M_\odot$  and dimensionless radius  $\bar{R} = R/10$  km. Although the above formula was derived for *nonrotating* stars, we use it as an upper bound, since the actual damping timescale for rapidly rotating stars is shorter. Above, we use the *mass of the remnant* (not of the individual components before merger) and we extract the equatorial radius of the remnant, neglecting its low-density envelope and consider the mass enclosed within this radius. For example, for the DD2 EoS we find an upper bound on the damping time scale of  $\sim 200$  ms for the remnant that results from the merger of two NSs with  $1.35 M_\odot$  each. We note that the applicability of the above formula is limited only to remnants for which it still gives positive values for the damping timescale, i.e. to remnants for which  $\frac{\bar{M}}{\bar{R}} < 1.56$ .

As an estimate for a *lower bound* on the damping timescale, we consider the following. In [100, 101] the damping timescale due to gravitational wave emission of the  $l = m = 2$   $f$ -mode in rapidly rotating stars was studied, assuming uniform rotation and the Cowling approximation. In particular, [101] used tabulated EoSs and estimated that the Cowling approximation overestimates the mode frequencies by up to 30%, while it underestimates damping timescales by up to a factor of three. Nevertheless, [101] found an empirical relation between the damping timescale  $\tau$  of a corotating  $f$ -mode in a uniformly rotating star and the corresponding damping timescale in a nonrotating model of *the same central density*. This relation shows that a star rotating at the mass-shedding limit will have a damping timescale which is  $\sim 1/10$  of the corresponding nonrotating model with the same central density. We find that for remnants that are far from the threshold to prompt collapse, the central density of the remnant remains comparable, within a factor of two, to the central density of one of the binary component before merger. Therefore, one can relate the damping timescale of the rotating remnant to the damping timescale of a nonrotating model with mass equal to the mass of one of the binary components before merger, through the empirical relation found in [101]. We consider this as an *approximate* lower bound, because the central density of the remnant is actually increasing somewhat, compared to the single star before merger, the actual damping timescale could be somewhat shorter, but at this level other uncertainties come into play and only a real calculation could give a precise result.

For example, for a  $1.35 + 1.35 M_\odot$  merger with the DD2 EoS, using Eq. (11) for a nonrotating  $1.35 M_\odot$  model, which has a radius of  $\sim 13.2$  km for this EoS, one obtains  $\tau_0 \sim 280$  ms, and applying the empirical formula of [101], this corresponds to  $\tau \sim 28$  ms for a uniformly rotating star at the mass-shedding limit. For the same mass but with the APR EoS, we estimate a lower bound

on the damping timescale of  $\sim 18$ ms; this is due to the smaller radius of 11.33 km for this model. Note that the estimates of the GW emission timescale of  $\sim 30 - 50$ ms in [14, 15] (which were based on the rate of angular momentum loss during simulations) fall within our estimated upper and lower bounds and are in fact closer to our lower bound.

The frequency of the corotating  $l = m = 2$   $f$ -mode levels off as the mass-shedding limit is approached (see [100–102]) and so does the damping timescale [101]. In reality, the remnant will rotate more rapidly than the mass-shedding limit for uniform rotation, but it is evident from [103] that the frequency remains practically constant, for reasonable values of the degree of differential rotation. Therefore, to a first approximation we will neglect the effect of differential rotation and assume that the reduction of the damping timescale by a factor of  $\sim 1/10$ , as obtained at the mass-shedding limit for uniform rotation, will also hold for hypermassive models with higher masses, but comparable central density.

Finally, one should also consider the indirect effect of nonzero temperature on the damping timescales, through the corresponding increase in radius. For the temperatures occurring in the remnants in our simulations this effect will be within the range of the upper and lower bounds considered above and so we do not treat it separately. This is based on the results of [104].

We construct additional hybrid waveforms in which we allow for the remnant to become more compact during the evolution in order to test the sensitivity of our results to such an effect. In general, the  $f$ -mode frequency scales approximately as  $\sqrt{M/R^3}$  [26, 27] and we consider the change of the frequency being mediated by a change of the remnant's radius. Here we assume that the loss of angular momentum by gravitational radiation is the dominant mechanism affecting the radius of the remnant while magnetic fields lead to a braking of the differential rotation on a timescale of  $\sim 100$  ms [96]. The loss of angular momentum during the damping timescale of  $\sim 200$  ms can be compared to the change of angular momentum in uniformly rotating neutron stars of constant rest mass. From this we obtain a rough estimate of the frequency change of about 5 per cent. We stress that mass loss counteracts the compactification of the remnant and that the frequency change is probably overestimated, in particular, for the hybrid waveforms with shorter damping timescales. We employ values of 5 and 0.0 per cent for the change of the dominant oscillation frequency per damping timescale. For shorter damping timescales a five per cent change represents a rather extreme case, which we choose by purpose to test the sensitivity of our method to such an extreme assumption.

Table III summarises the parameters of the hybridized waveforms used in this study.

Hybrid	EoS	$\Delta f/f$ [%]	$\tau_0$ [ms]
hlAPR <sup>†</sup>	APR	0.00	180
hlAPR <sup>*</sup>	APR	0.05	200
hsAPR <sup>†</sup>	APR	0.00	18
hsAPR <sup>*</sup>	APR	0.05	18
hlDD2 <sup>†</sup>	DD2	0.00	200
hlDD2 <sup>*</sup>	DD2	0.05	200
hsDD2 <sup>†</sup>	DD2	0.00	28
hsDD2 <sup>*</sup>	DD2	0.05	28

TABLE III. Characteristics of the hybridized waveforms used in this study. Daggers (<sup>†</sup>) and asterixes (<sup>\*</sup>) indicate whether the analytic part of the waveform is a stationary (in frequency) ring-down or a decaying chirp, where the frequency increases by the percentage shown in the  $\Delta f/f$  column. The  $\tau_0$  column indicates the e-folding time for the decay of the analytic signal.

### 3. GW Signal Simulations

The GW polarizations  $h_+$  and  $h_\times$  are computed from the second time derivative of the quadrupole moment of the source  $\ddot{I}$ , which is obtained from the numerical simulations. The quantity  $h_+ - ih_\times$  can be decomposed into modes with spin weighted spherical harmonics  ${}^sY_{\ell m}(\theta, \phi)$  of weight  $-2$ :

$$h_+ - ih_\times = \frac{1}{D} \sum_{\ell=2}^{\infty} \sum_{m=-\ell}^{\ell} {}^{-2}Y_{\ell m}(\theta, \phi) H_{\ell m}(t). \quad (12)$$

The expansion parameters  $H_{\ell m}(t)$  are complex functions of the retarded source time  $t$ . The  $H_{2m}$ , where  $\ell = 2$  is the quadrupole mode, may be expressed in terms of the second time derivatives of the Cartesian components of the mass quadrupole moment  $\ddot{I}$  as,

$$H_{20} = \sqrt{\frac{32\pi}{15}} \frac{G}{c^4} \left[ \ddot{I}_{zz} - \frac{1}{2} (\ddot{I}_{xx} + \ddot{I}_{yy}) \right] \quad (13)$$

$$H_{2\pm 1} = \sqrt{\frac{16\pi}{5}} \frac{G}{c^4} (\mp \ddot{I}_{xz} + i \ddot{I}_{yz}) \quad (14)$$

$$H_{2\pm 2} = \sqrt{\frac{4\pi}{5}} \frac{G}{c^4} (\ddot{I}_{xx} - \ddot{I}_{yy} \mp 2i \ddot{I}_{xy}). \quad (15)$$

Figures 5 and 6 show the catalogue of waveforms used in this study, assuming a distance of 20 Mpc and optimal source sky-location and orientation. We discuss the characteristics of these waveforms in section IV A.

The polarisations  $h_+$  and  $h_\times$  constructed from the quadrupole moments from each simulation were superimposed on the recolored data streams from each detector after the appropriate projection onto the sky for a given sky location, inclination and polarization:

$$h(t) = F_+(\boldsymbol{\Omega}, \psi) h_+(t) + F_\times(\boldsymbol{\Omega}, \psi) h_\times(t), \quad (16)$$

where  $\boldsymbol{\Omega}$  is the sky-location,  $\psi$  is the GW polarization angle and  $F_+$  and  $F_\times$  are the detector antenna

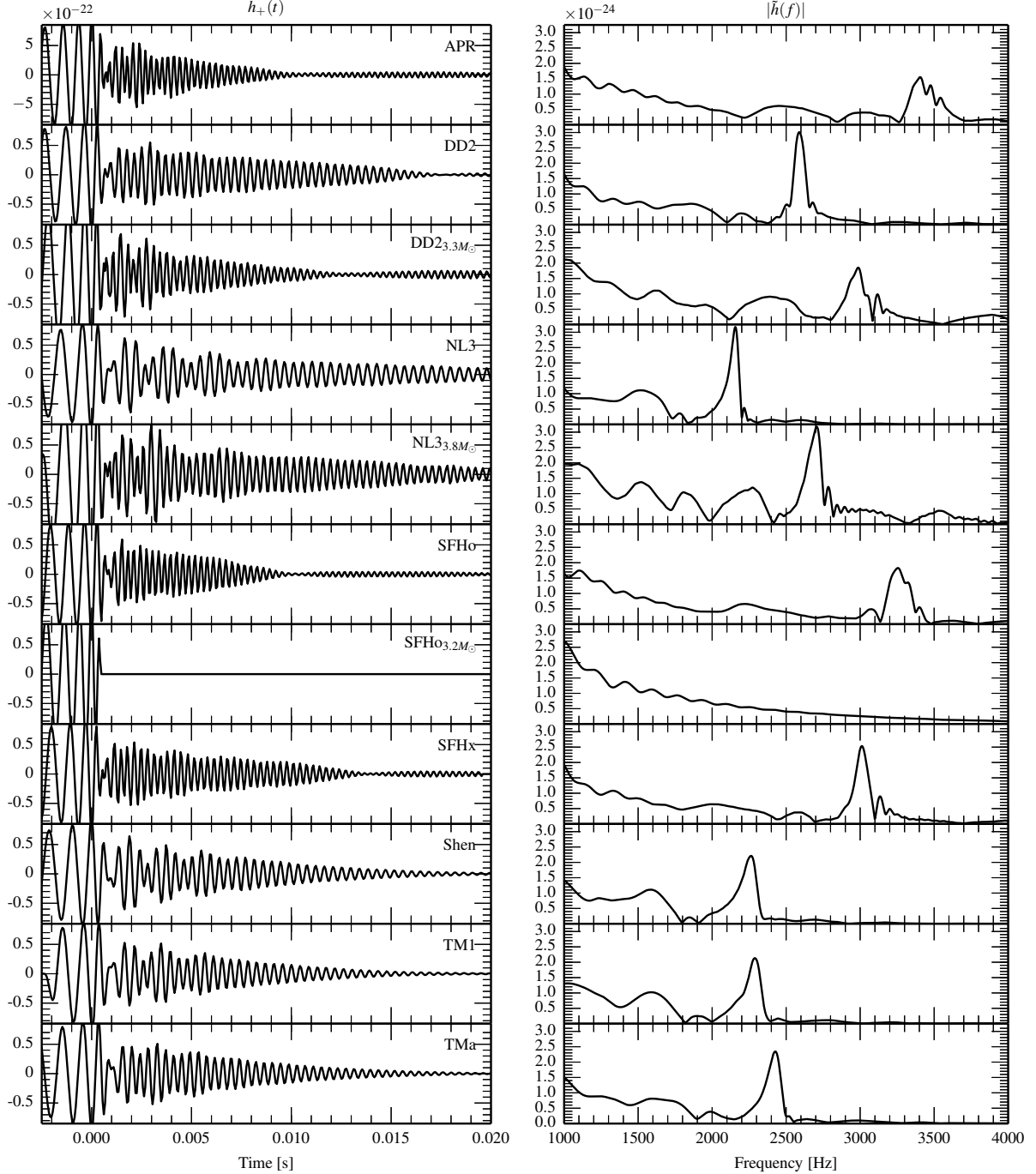


FIG. 5. The catalogue of waveforms used in this study. *Left column:* The time series of the plus polarization of the gravitational waves for a source at 20 Mpc. *Right column:* The amplitude spectral density of the characteristic strain (solid line) for an optimally located and oriented source and the aLIGO design sensitivity (dashed line).

responses, defined in [58]. The inclination dependence enters through the spherical harmonics in equation 12. Note that, the amplitude of the waveforms is scaled up by 40% before being injected to account for the amplitude underestimate from extraction in the quadrupole approximation [15, 27].

We refer to these signal simulations as *injections*. Injections are added approximately every 60 seconds with a uniform random offset within a 10 second window. This placed all injections far enough apart that the whitening and noise estimation procedures, which use data surrounding each injection, is never affected by a neighbor-

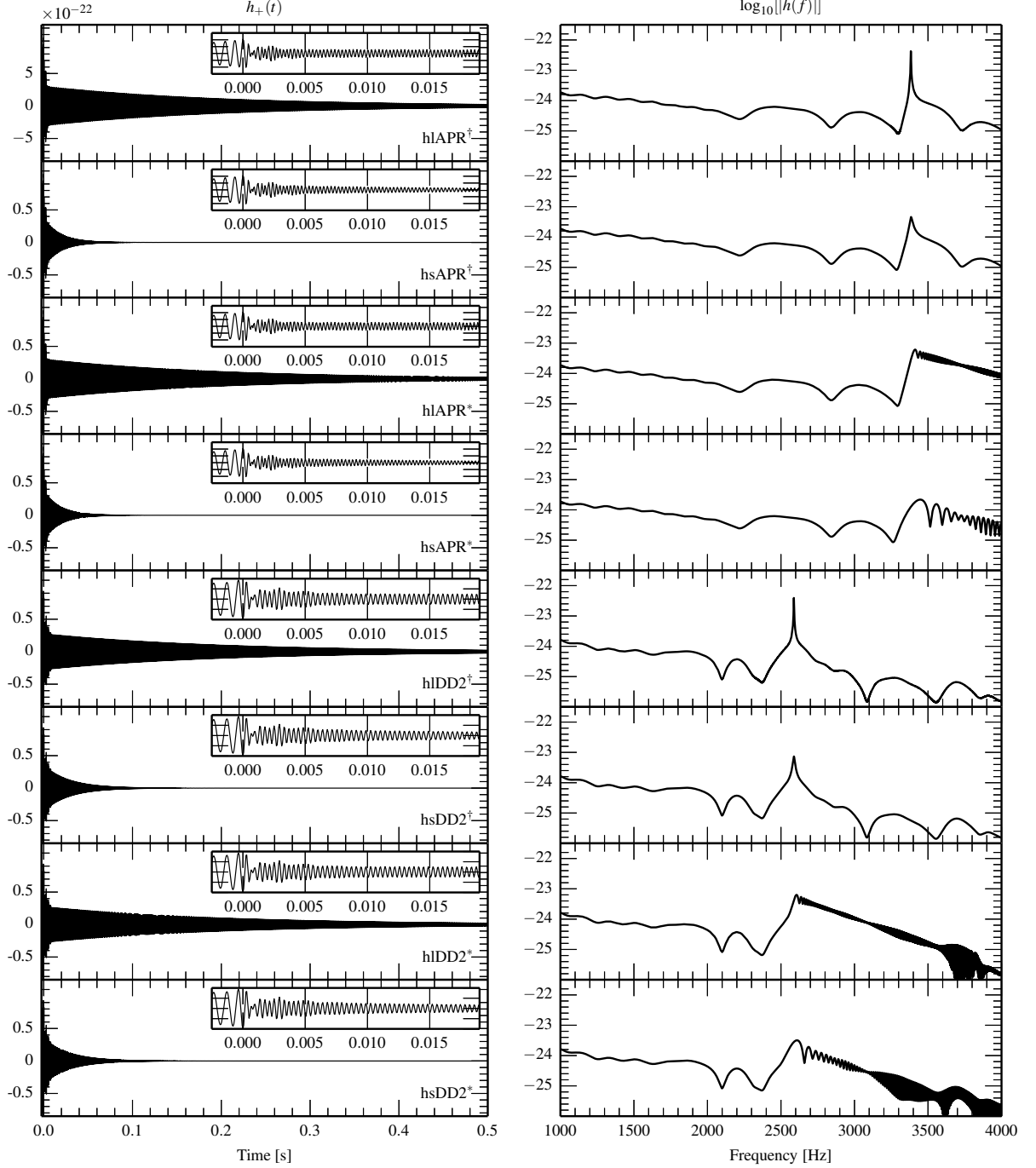


FIG. 6. The hybridized waveforms used in this study. *Left column:* The time series of the plus polarization of the gravitational waves for a source at 20 Mpc. Insets show the early evolution of the signal for comparison with the original waveforms shown in figure 5. *Right column:* The amplitude spectral density of the characteristic strain (solid line) of the hybridized waveforms for an optimally located and oriented source and the aLIGO design sensitivity (dashed line).

ing injection. The injections were distributed isotropically over the sky with randomized source inclinations (uniform in  $\cos \iota$ ) and polarizations (uniform in polarization angle  $\Psi$ ). Thus, all results quoted in this study are averaged over sky location and source orientation. The

distances of the injections are distributed uniformly in [0.5, 8] Mpc for the purely numerical waveforms and in [0.5, 15] Mpc for the hybridized waveforms. These distributions are chosen to cover the range of detection scenarios and are not intended to correspond to astrophysical



scenarios. This procedure was repeated ten times resulting in a population of approximately 53000 injections for each waveform type. The results of the injections are then binned in distance and used to estimate detection probability as a function of distance as described in § IV B.

We conduct separate simulation campaigns for each of the waveforms in our catalogue (i.e., figure 5, table IV) and characterise the results for each waveform separately.

### C. Background Estimation & Detection Criterion

Following the approach used in recent searches for GW transients [49, 50] and as described in section II A, triggers arising from the CWB analysis are ranked by their coherent network amplitude,  $\eta$ . The statistical significance of CWB triggers is determined from the distribution  $\eta$  in the absence of GW signals, the background distribution, which is estimated by time-shifting individual detector data streams relative to each other by an amount greater than the light travel time between each detector. This ensures no GW signal is present in the background data set, and also provides a convenient means to increase the background statistics of a relatively short data segment. Fifty such time shifts in increments of 1 second are applied in this study. This background analysis assigns a false alarm rate (FAR) to the CWB triggers. This rate is then interpreted as a  $p$ -value by assuming some observation time. For the purposes of this study, we assume an observation time of  $T_{obs} = 100$  ms. This represents a conservative estimate of the time of coalescence measured from the inspiral signal.

We place a threshold on the statistical significance required for detection of  $3\text{-}\sigma$ . The network configuration chosen for this analysis corresponds to an expected BNS detection rate of  $\mathcal{O}(100)$  events / year. For a  $3\text{-}\sigma$  significance then, with 100 trials, triggers with  $p$ -value  $p < 10^{-5}$  are regarded as GW detection candidates. Finally, the assumed observation time of  $T_{obs} = 100$  ms results in a FAR threshold of  $10^{-4}$  Hz.

## IV. DETECTABILITY STUDY

We now discuss the prospects for the detection and measurement of the post-merger GW signal with the algorithm described in section II.

### A. Waveform Characteristics & Expected Detectability

We begin by considering the expected detectability of the post-merger signal with an optimal matched-filter. While matched-filtering may not be realistic, due to the scarcity of templates and high computational costs, it

provides an estimate for the best-case sensitivity to these systems in stationary, Gaussian data.

If the form of the expected GW signal in the detector is known *a priori*, the optimal detection statistic is the matched-filter signal-to-noise ratio (SNR)  $\rho$ :

$$\rho^2 = 4\Re \int_{f_{\text{low}}}^{f_{\text{upp}}} \frac{\tilde{d}(f)\tilde{h}^*(f)}{S(f)} df, \quad (17)$$

where  $\tilde{h}(f)$  is a template for the expected GW signal,  $\tilde{d}(f)$  is the Fourier transform of the data,  $S(f)$  is the one-sided noise power spectral density and  $f_{\text{low}}$  and  $f_{\text{upp}}$  are lower and upper bounds on the searched frequency range [105].

Under the assumption of Gaussian noise and in the absence of a signal,  $\rho^2$  follows a central  $\chi^2$ -distribution with  $k = 2$  degrees of freedom. The SNR threshold  $\rho_{\text{thresh}}$  which corresponds to a false alarm probability of  $10^{-5}$  is found from the survival function of the SNR distribution in Gaussian noise, evaluated at the chosen false alarm probability:

$$\text{FAP} = 1 - P_{\chi^2}(\rho^2 \leq \rho_{\text{thresh}}^2 | k = 2)^{N_t}. \quad (18)$$

In this equation,  $N_t$  is a trials factor introduced by searching over a template bank. For the most optimistic estimate, we assume the signal is known exactly and only a single waveform template is required, so that  $N_t = 1$ <sup>2</sup>. For  $\text{FAP} = 10^{-5}$ , eq. 18 yields  $\rho_{\text{thresh}} = 4.8$ . Table IV lists the SNR for the waveform of this study, evaluated at 20 Mpc. Two SNRs are reported:  $\text{SNR}_{\text{full}}$ ; the SNR evaluated over the full frequency range of [1.5, 4] kHz and which is used to determine the detectability of the signal and  $\text{SNR}_{\text{peak}}$  which is the SNR evaluated over a narrow frequency range around the dominant high-frequency peak and indicates the relative strength of the post-merger oscillation as compared with the full late-inspiral, merger and post-merger signal.

The distance-reach of a search is often characterized by its *horizon distance*  $D_h$ , the distance at which an optimally-oriented source yields an SNR at least as large as the detection threshold. Since SNR scales inversely with distance, the horizon distance is obtained by rescaling the fiducial 20 Mpc to that distance which yields  $\text{SNR}_{\text{full}} \approx 5$ .

Following [61], we define the effective range  $\mathcal{R}_{\text{Opt}}$  of this hypothetical, optimal search as the radius enclosing a spherical volume  $V$  such that the rate of detections from a homogenous, isotropic distribution of sources with rate density  $\dot{\mathcal{N}}$  is  $\dot{\mathcal{N}}V$ . For an elliptically polarized source [106] the effective range  $\mathcal{R}_{\text{Opt}} \approx D_h/2.26$ , where the factor 2.26 accounts for the average over all sky-locations and orientations. Table IV lists the optimal effective range  $\mathcal{R}_{\text{Opt}}$  for each waveform in the catalogue,

<sup>2</sup> Note that this also implies that the sky-location and time of the signal are known.

calculated from the noise PSD of a single aLIGO instrument at design sensitivity. An optimal search with  $X$  detectors with comparable sensitivity will be a factor  $\sqrt{X}$  more sensitive than the single detector search [6]. In table IV, we also report the expected effective range for an optimal search in Gaussian noise assuming a network of 3 instruments with the aLIGO design sensitivity. Figure 7 summarises the theoretically-achievable effective range for each waveform and compares this with the result from the CWB Monte-Carlo analysis reported in the next section.

The expected detection rate  $\dot{N}_{\text{det}}^{\text{Opt}}$  is obtained by considering the number of Milky Way Equivalent Galaxies (MWEGs) within the effective range<sup>3</sup> and the estimated BNS coalescence rate. Assuming the coalescence rate  $\dot{N} = 100 \text{ MWEG}^{-1} \text{ Myr}^{-1}$  [6], we find  $\dot{N}_{\text{det}}^{\text{Opt}} \sim 0.01\text{--}0.1 \text{ year}^{-1}$ , in reasonable agreement with previous estimates [14, 17, 20, 23, 27, 29, 31].

Finally, table IV reports the energy emitted in GWs,  $E_{\text{GW}}$  and the peak post-merger frequency, where appropriate. The energy  $E_{\text{GW}}$  was calculated from a numerical integration of:

$$E_{\text{GW}} = \frac{\pi c^3}{4G} D^2 \int_{-1}^1 d(\cos \iota) \int_0^{2\pi} d\lambda \quad (19)$$

$$\times \int_{-\infty}^{\infty} df \left[ \frac{(1 + \cos^2 \iota)^2}{4} + \cos^2 \iota \right] f^2 |\tilde{h}(f)|^2$$

$$= \frac{8\pi^2 c^3}{5G} D^2 \int_{-\infty}^{\infty} df f^2 |\tilde{h}(f)|^2.$$

## B. Monte-Carlo Study

### 1. Detectability

For a more realistic estimate, we performed a Monte-Carlo study with realistic data and the CWB algorithm, as presented in section II. We define the analysis effective range  $\mathcal{R}_{\text{CWB}}$  as the radius of a volume  $V$  such that the rate of detections is  $\dot{N}V$ , where  $V$  is:

$$V = \int_0^{\infty} dr 4\pi r^2 \epsilon(r) \quad (20)$$

and  $\epsilon(r)$  is the probability of detecting the post-merger signal at distance  $r$ , averaged over sky-location and orientation.  $\epsilon(r)$  is referred to as the *efficiency* of the search, and is determined by binning the injections in distance and counting the number of found injections  $k$  out of  $N$  trials. Assuming a uniform prior on the efficiency, the posterior probability density distribution for  $\epsilon$  is,

$$P(\epsilon|k, N) = \frac{(N+1)!}{(N-k)!k!} \epsilon^k (1-\epsilon)^{N-k}. \quad (21)$$

<sup>3</sup> Found from figure 1 of [6]

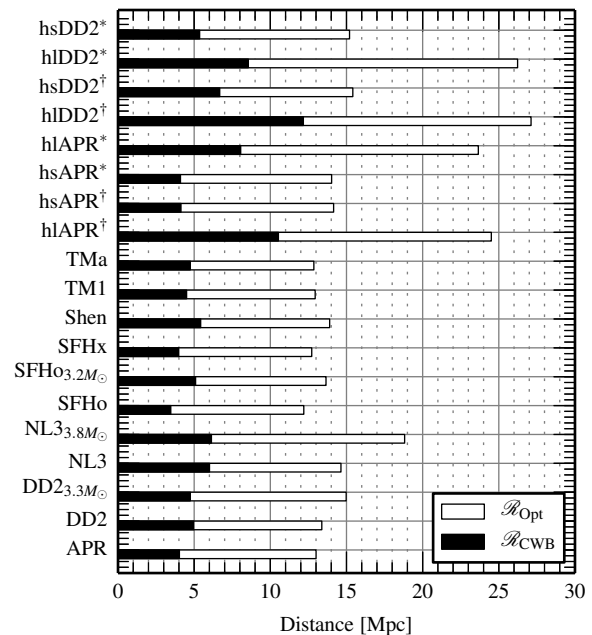


FIG. 7. The effective ranges for each waveform for an idealized optimal matched-filter analysis strategy ( $\mathcal{R}_{\text{Opt}}$ ) and the CWB Monte-Carlo study ( $\mathcal{R}_{\text{CWB}}$ ). Both ranges are evaluated at assuming a false alarm probability of  $10^{-5}$ . Differences in the ranges for each waveform are consistent with the difference in the optimal SNR.

We estimate the efficiency from its expectation value, given  $k$  detections in  $N$  simulations at distance  $r$ ,

$$\langle \epsilon \rangle = \int \epsilon P(\epsilon|k, N) d\epsilon \quad (22)$$

$$= \frac{k+1}{N+2}. \quad (23)$$

The effective range is the radius of a sphere of volume  $V$ :

$$\mathcal{R}_{\text{CWB}} = \left[ 3 \int_0^{\infty} dr r^2 \epsilon(r) \right]^{1/3}. \quad (24)$$

We report the values for  $\mathcal{R}_{\text{CWB}}$  for each waveform in the catalogue in figure 7 and in table V. We find that the range of the CWB analysis is approximately 60–70% smaller than an optimal search with perfect knowledge of the waveform in stationary, Gaussian noise. This also implies a reduction of the expected detection rate, with  $\dot{N}_{\text{det}}^{\text{CWB}} \sim 10^{-3}\text{--}0.1 \text{ events/year}$ , as listed in table V.

### 2. Waveform Classification & Parameter Recovery

Figures 8, 9 and 11 summarize the results of this analysis, marginalized over all extrinsic parameters, such as distance, sky location and source orientation. We characterize the performance of the classification scheme in

Waveform	$\text{SNR}_{\text{full}}$	$\text{SNR}_{\text{peak}}$	$\mathcal{R}_{\text{Opt}}$ [Mpc]	$\dot{N}_{\text{det}}^{\text{Opt}}$ [year <sup>-1</sup> ]	$E_{\text{GW}}$ [ $M_{\odot}$ ]	$E_{\text{GW}}^{\text{peak}}$ [ $M_{\odot}$ ]	$f_{\text{peak}}$ [Hz]
APR	4.07	1.66	13.00	0.04	0.09	0.05	3405.40
DD2	4.19	3.13	13.38	0.04	0.07	0.06	2588.60
DD2 <sub>3.3M<math>\odot</math></sub>	4.69	2.00	14.98	0.06	0.09	0.04	2987.00
NL3	4.58	3.34	14.64	0.05	0.04	0.03	2156.80
NL3 <sub>3.8M<math>\odot</math></sub>	5.89	3.46	18.82	0.12	0.14	0.08	2706.60
SFHo	3.82	2.06	12.20	0.03	0.08	0.06	3255.20
SFHo <sub>3.2M<math>\odot</math></sub>	4.28	-	13.65	0.04	0.04	-	-
SFHx	3.98	2.44	12.72	0.04	0.09	0.06	3011.40
Shen	4.35	2.96	13.89	0.05	0.04	0.03	2263.20
TM1	4.05	2.73	12.94	0.04	0.04	0.03	2288.60
TMa	4.03	2.84	12.86	0.04	0.05	0.04	2426.80
hlAPR <sup>†</sup>	7.67	5.54	24.51	0.25	0.76	0.49	3383.40
hsAPR <sup>†</sup>	4.43	2.00	14.15	0.05	0.14	0.06	3384.20
hlAPR*	7.41	4.05	23.66	0.23	0.82	0.27	3412.60
hsAPR*	4.39	2.23	14.02	0.05	0.14	0.09	3447.20
hlDD2 <sup>†</sup>	8.49	6.74	27.12	0.30	0.38	0.26	2587.80
hsDD2 <sup>†</sup>	4.83	3.32	15.42	0.06	0.10	0.06	2588.00
hlDD2*	8.21	6.11	26.23	0.28	0.41	0.22	2606.00
hsDD2*	4.76	3.28	15.20	0.06	0.11	0.06	2609.00

TABLE IV. Characteristics of the waveforms used in this study. Unless otherwise indicated in the subscript, the total mass is  $2.7M_{\odot}$  and all systems have a symmetric mass configuration (see § III B 1). Signal to noise ratios are evaluated for an optimally oriented source at 20 Mpc. Fields denoted “full” refer to quantities evaluated over the full frequency range used for detection [1.5, 4.0] kHz. Fields denoted “peak” refer to those quantities evaluated in a narrow range around the dominant high-frequency spectral peak (a  $2\sigma$  width around the best fitting Gaussian).  $\mathcal{R}_{\text{Opt}}$  is the effective range of an optimal matched-filter search, assuming a  $3\text{-}\sigma$  statistical significance and  $\mathcal{O}(100)$  BNS-inspiral triggers;  $\dot{N}_{\text{det}}^{\text{Opt}}$  is the expected number of post-merger signal detections for a search with this effective range. The energy,  $E_{\text{GW}}$  is the energy carried by the GW signal assuming elliptical polarization and computed according to equation 19.  $f_{\text{peak}}$  is the frequency of the highest peak in the signal power spectrum. Note that the  $3.2M_{\odot}$  SFHo waveform exhibits prompt collapse so the post-merger characteristics are undefined here.

terms of the *classification accuracy*, which is the probability that the outcome of the merger is correctly identified as prompt (SFHo<sub>3.2M $\odot$</sub>  simulation) or delayed collapse (all other simulations). This is evaluated as an efficiency using equation 22, where  $k$  is now the number of correctly classified signals and  $N$  is the total number of detected signals.

In general, we find that the classification accuracy is better than 95%; the classification algorithm selects the correct post-merger scenario when confronted with both PMNS and prompt-collapse waveforms. We note, however, that three of the PMNS waveforms studied, APR, DD2<sub>3.2M $\odot$</sub>  and SFHo, yield lower classification accuracies of  $\sim 70\%$ , as the SNR of the post-merger peak in these models comprises a significantly lower fraction of the full waveform. In the cases where the waveform is mis-classified, only the low frequency component of the spectrum is loud enough to be reconstructed and no post-merger peak is visible.

Figure 9 summarizes the accuracy of the post-merger frequency determination for our suite of PMNS waveforms. Figure 9a shows the recovered frequency as a function of the target frequency for each waveform. Figure 9b illustrates the accuracy of the frequency measurement in

terms of the median value and interquartile range of the absolute deviation from the nominal target value:

$$\delta f_{\text{peak}} \equiv \left| f_{\text{peak}} - f'_{\text{peak}} \right|. \quad (25)$$

The median error lies in  $\delta f_{\text{peak}} \sim [4, 15]$  Hz for the purely numerical waveforms and  $\delta f_{\text{peak}} \sim [2, 12]$  Hz for the hybridized waveforms. We find that the frequency measurements are most accurate for waveforms with the most clearly defined and symmetric post-merger peaks.

Given the relative likelihood that BNS coalescence results in the formation of a PMNS for a wide variety of EoS and canonical NS masses ( $m_1 = m_2 = 1.35M_{\odot}$ ), it is natural to ask whether the classification stage is necessary. We find that the classification stage significantly improves the robustness of the frequency estimation, particularly for waveforms where the post-merger peak represents only a small fraction of the total power in the waveform (i.e., APR, DD2<sub>3.2M $\odot$</sub>  and SFHo). To illustrate this, figure 10 shows the cumulative distribution of the frequency error  $\delta f_{\text{peak}}$  for the APR waveform, with and without the classification procedure. If we simply assume that the merger results in PMNS formation, the best-fitting Gaussian component for the spectrum (see

Waveform	$\mathcal{R}_{\text{CWB}}$ [Mpc]	$\dot{N}_{\text{det}} \times 10^{-2}$ [year $^{-1}$ ]	Classification Accuracy	$\delta f_{\text{peak}}$ [Hz]	$\delta \tilde{R}_{1.6}$ [m]
APR	4.03	0.37	0.67	10.96	131.69
DD2	4.98	0.58	0.96	5.48	188.16
DD2 <sub>3.3M<math>\odot</math></sub>	4.74	0.57	0.69	13.63	-
NL3	6.01	0.64	0.97	9.06	150.24
NL3 <sub>3.8M<math>\odot</math></sub>	6.13	0.64	0.95	15.03	-
SFHo	3.46	0.25	0.75	6.87	89.49
SFHo <sub>3.2M<math>\odot</math></sub>	5.09	0.59	0.95	-	-
SFHx	3.99	0.36	0.95	3.83	242.07
Shen	5.43	0.62	0.96	15.72	234.13
TM1	4.50	0.55	0.95	10.05	175.38
TMa	4.75	0.57	0.97	12.43	30.55
hlAPR $^\dagger$	10.53	2.15	0.97	1.91	168.65
hsAPR $^\dagger$	4.13	0.43	0.77	4.15	162.71
hsAPR $^*$	4.10	0.41	0.75	9.55	59.79
hlAPR $^*$	8.05	1.11	0.96	9.66	106.93
hlDD2 $^\dagger$	12.17	3.21	0.99	1.66	167.40
hsDD2 $^\dagger$	6.68	0.71	0.98	1.02	169.32
hlDD2 $^*$	8.55	1.23	0.98	12.40	242.25
hsDD2 $^*$	5.36	0.61	0.96	4.73	229.28

TABLE V. Results summary showing effective range to which the CWB analysis is sensitive and the expected detection rate assuming the “realistic” BNS coalescence rate given in [6]. *Classification accuracy* gives the probability that the post-merger scenario (delayed vs prompt collapse) is correctly identified. The delayed collapse waveforms are also characterised in terms of the median error in the peak frequency measurement and, where appropriate, the median error in the estimation of  $R_{1.6}$ .

equation 6) frequently lies at much lower frequencies than the true post-merger peak, which may not be detected and reconstructed by CWB at all, leading to serious errors in the the frequency estimation. Indeed, we find that the 90<sup>th</sup>-percentile of the frequency error with no classification stage is 1477 kHz. This value falls to just 50 Hz when we include the classification step. We find similar results for the DD2<sub>3.2M $\odot$</sub>  and SFHo waveforms. The classification algorithm is, therefore, an integral part of this analysis and helps to ensure that there is reasonable evidence for the existence of the post-merger spectral peak prior to estimating its frequency.

We conclude by considering the accuracy of the determination of the radius of a reference 1.6 M $\odot$  neutron star, using the measured  $f'_{\text{peak}}$  and the fit of equation 1 from [27]. This fit is derived for systems with total mass 2.7 M $\odot$ . We thus restrict this aspect of the analysis to those simulations with  $M_{\text{tot}} = 2.7M_{\odot}$ . It is worth noting that one can still expect a correlation between  $f_{\text{peak}}$  and the radius of a reference neutron star for different mass configurations but further systematic studies similar to those in [27] will be necessary to obtain a fit for the precise form of this relationship. Figure 11b shows the distributions of the error in the measured radius, defined as:

$$\delta R_{1.6} = \left| R_{1.6} - R'_{1.6} \right|, \quad (26)$$

where  $R'_{1.6}$  is the radius from equation 1 and the mea-

sured post-merger frequency  $f'_{\text{peak}}$ . We find the median radius error lies in  $\delta R_{1.6} \sim [30, 250]$  m, where the smallest (largest) error is associated with the TMa (SFHx) waveform.

## V. CONCLUSION

This paper presents the first systematic study of the expected detectability of high-frequency bursts of GWs from the merger and post-merger phase of binary neutron star coalescence in the second generation of ground based detectors, using the Coherent WaveBurst algorithm for unmodeled transient searches followed by a classification scheme.

We determine the distance reach, and hence, the expected detection rates for the CWB analysis through a large scale Monte-Carlo study where simulated post-merger GW signals are injected into realistic non-Gaussian, non-stationary detector data which has been recolored such that the noise power-spectral density matches the design goals of aLIGO and AdV.

The results from the CWB Monte-Carlo study are compared with the expected range and rates for a completely optimal matched-filter analysis assuming stationary, Gaussian noise. We find the effective range of the CWB analysis is  $\mathcal{R}_{\text{CWB}} \sim 4\text{-}11$  Mpc, depending on the energy-content of the post-merger GW signal,



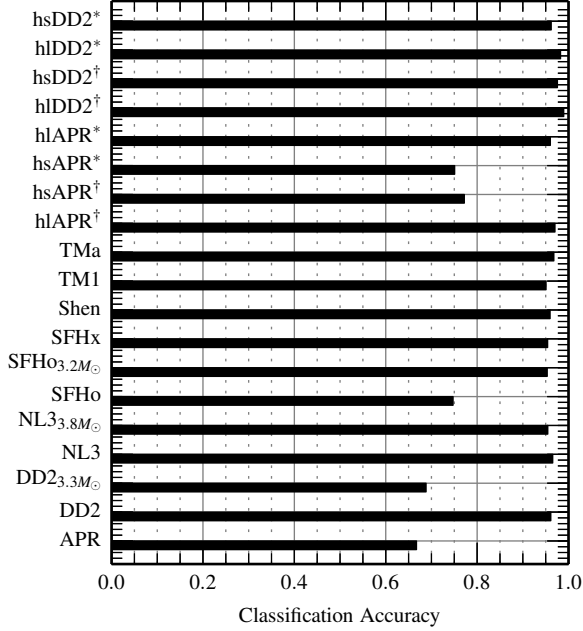
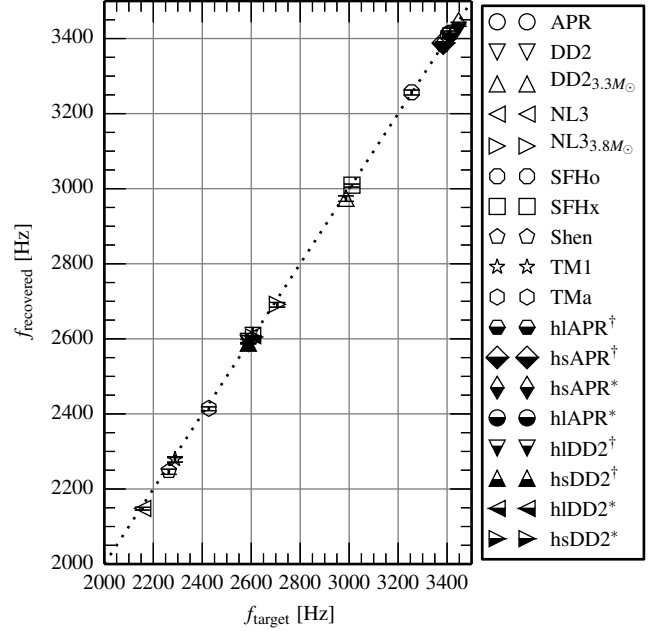


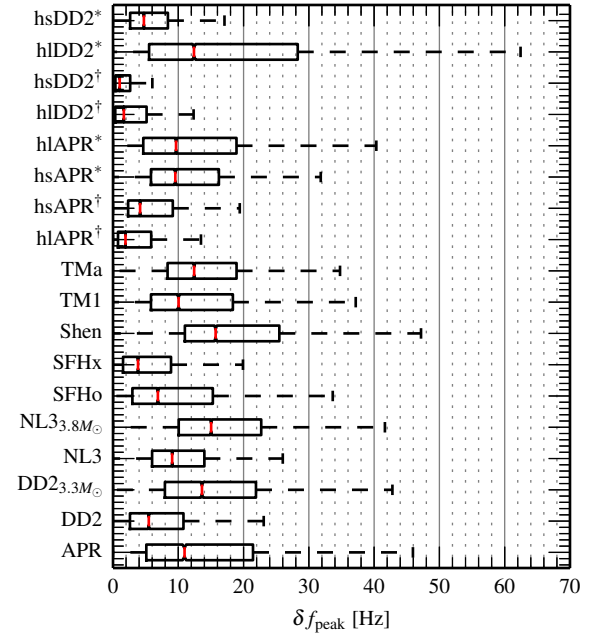
FIG. 8. Classification accuracy: the probability that the post-merger scenario is correctly identified. Of these models,  $\text{SFHo}_{3.2M_\odot}$  exhibits prompt collapse to a black hole; all other simulations result in PMNS formation.

corresponding to an expected detection rate  $\dot{N}_{\text{det}}^{\text{CWB}} \sim 10^{-3}$ -0.1 events per year, assuming the ‘realistic’ coalescence rate  $\dot{N} = 100 \text{ MWEg}^{-1} \text{ Myr}^{-1}$  from [6]. If the waveform is known exactly, permitting the use of an optimally-matched filter, the post-merger signals considered in this paper may be detectable within a sphere of radius  $\mathcal{R}_{\text{Opt}} \sim 13$ -27 Mpc, depending on the energy-content of the post-merger GW signal, corresponding to an expected detection rate  $\dot{N}_{\text{det}}^{\text{Opt}} \sim 0.03$ -0.3 events per year. Both results assume that the threshold required for detection corresponds to a false alarm probability of  $p = 10^{-5}$ , as required for a statistical significance of approximately  $3\sigma$  for the follow-up of  $\mathcal{O}(100)$  events where the inspiral part of the GW signal has been detected.

While there is nearly an order of magnitude difference between the sensitivity of the CWB analysis and the expectation for the idealised matched-filter, it is important to stress that the optimal sensitivity is highly unlikely to be realised in practice; even if there was a sufficiently accurate analytic form for the merger/post-merger signal which would facilitate the construction of a matched-filter, the start time of the signal, the sky-location and the intrinsic parameters of the source would still be unknown. Searching over the unknown parameter space introduces a trials factor into the SNR distribution, reducing the sensitivity of the search. Furthermore, real detector data is rarely Gaussian or stationary, which tends to increase the threshold required for detection further. The CWB analysis, by contrast, makes no assumptions regarding waveform morphology, uses an



(a) Median recovered frequencies



(b) Error in recovered frequencies

FIG. 9. Frequency recovery for the PMNS waveforms. *Top panel*: the median recovered frequency as versus the target peak frequency of the waveform. Half-filled symbols indicate hybridized waveforms (see sec III B 2). *Bottom panel*: the median (red lines), interquartile ranges (boxes) and the minimum and maximum values within  $1.5\times$  the interquartile range of the absolute error in the frequency determination for each waveform.

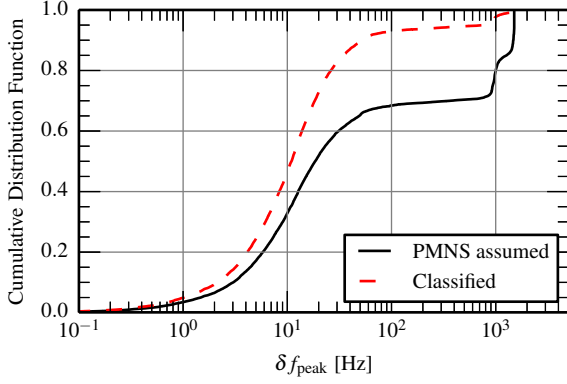
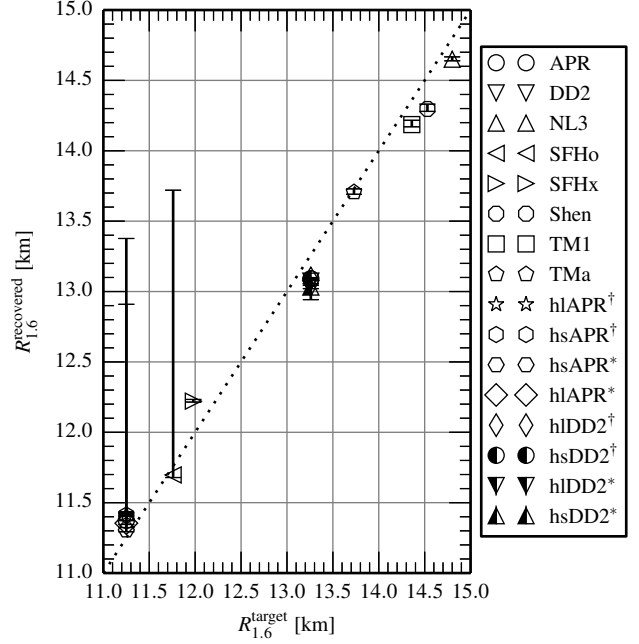


FIG. 10. The cumulative probability distribution of the absolute error in the determination of peak frequency for APR waveforms. The red, dashed trace shows the frequency error after we have applied our classification scheme (see section II B).

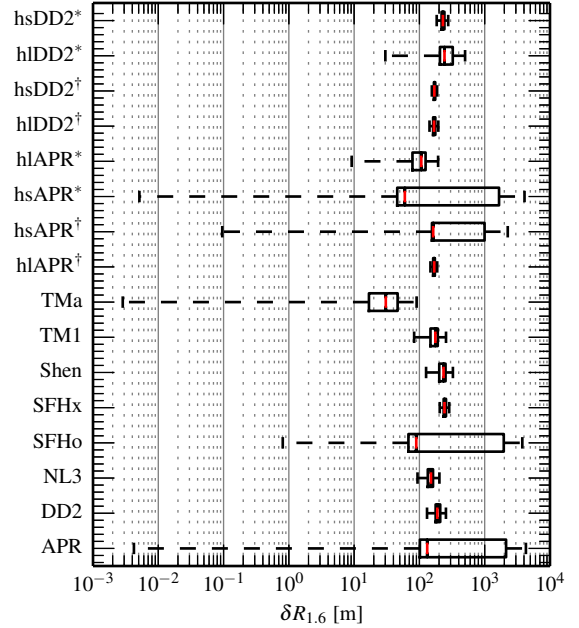
existing and well-tested data analysis pipeline and uses recoloured, initial-detector data which may plausibly be regarded to share the characteristics of advanced detector data. The optimal and CWB estimates may therefore be regarded as absolute upper and realistic lower bounds on the detectability of high-frequency GW signals from binary neutron star coalescence keeping in mind that the strength of the GW emission is not exactly known from numerical simulations.

We have also developed and demonstrated the efficacy of a simple model-selection and parameter estimation algorithm which distinguishes between the post-merger scenarios of prompt- and delayed-collapse to a black hole. This procedure, which has negligible computational cost as compared with the CWB analysis itself, assumes that any statistically significant high-frequency signal power following a binary neutron star inspiral is due to the merger/post-merger GW emission from the coalescence. For delayed collapse, we expect the reconstructed waveform to resemble a power-law decay with a Gaussian peak somewhere in  $\sim [2, 4]$  kHz, while no such peak is expected in the case of prompt-collapse to a black hole. We deploy the Bayesian Information Criterion to select between these models and find that, for most of the waveforms considered in this study, the probability of correctly identifying the post-merger scenario is greater than 95%. Delayed collapse waveforms in which the post-merger spectral peak comprises a smaller fraction of the total SNR prove harder to correctly classify since the spectrum is dominated by power from the late inspiral and merger as is the case with prompt collapse.

When the outcome of the merger is identified as delayed-collapse, the reconstruction analysis also returns the maximum-likelihood estimate of the center frequency for the Gaussian peak which we identify with the dominant post-merger oscillation frequency. We find that the typical magnitude of the error in this determination of



(a) Median recovered radii



(b) Error in recovered radii

FIG. 11. Radius recovery for the waveforms exhibiting delayed collapse: *Top panel*: the median recovered radius versus the target radius for a  $1.6M_{\odot}$  star with that EoS. *Bottom panel*: the median (red lines), interquartile ranges (boxes) and the minimum and maximum values within  $1.5\times$  the interquartile range of the absolute error in the radius determination for each waveform.

the peak frequency is  $\delta f_{\text{peak}} \sim 1\text{-}10\text{ Hz}$ , with the highest accuracy corresponding to waveforms in which the SNR is dominated by the contribution from the post-merger oscillations. In addition, the model selection stage used to distinguish prompt and delayed collapse increases the robustness of this frequency estimation by ensuring that there is indeed evidence for post-merger oscillations before attempting to measure their dominant frequency content.

Finally, following [27], we use the measured peak frequency to estimate the radius of a  $1.6 M_{\odot}$  neutron star and compare the result to the true radius of such a star with each waveform’s equation of state. Using the fit described in [27] (i.e., equation 1), we find that the typical magnitude of the error in this radius estimate is  $\delta R_{1.6} \sim 100\text{-}200\text{ m}$ , where the dominant source of error is in the fit itself associated with the scatter of the fitted model results rather than the measurement uncertainty. As remarked upon in section IV B 2, these estimates for the error in the recovered radius are based on the fit for a specific set of simulations (symmetric mass configuration with a total mass of  $2.7 M_{\odot}$ ) where the  $f_{\text{peak}}\text{-}R_{1.6}$  relationship has been carefully studied. Further surveys of the post-merger waveform, similar to that in [27], will be important to obtain relationships similar to the  $f_{\text{peak}}\text{-}R_{1.6}$  correlation for a variety of mass configurations and to account for different approaches and detailed physics used in various modelling codes.

We see then that the prospects for high-frequency searches for the post-merger signal following BNS coalescence rely on serendipitous nearby events and optimistic coalescence rates. While such a scenario may be unlikely, even in the advanced detector era, it is difficult to overstate the rewards of the detection and characterisation of the post-merger signal. Indeed, as we have shown in this work, the combination of very simple modelling of the signal spectrum and existing data analysis techniques allows one to correctly identify the post-merger scenario and, in the case of delayed collapse, accurately

measure the dominant post-merger oscillation frequency. Furthermore, refinements and advances in data analysis ranging from modifications such as improved time-frequency clustering and choice of basis for the CWB algorithm used in this study, to novel Bayesian techniques for the robust detection and characterisation of un-modelled signals (e.g., [107, 108]) may lead to significant improvements in the prospects for detecting the high-frequency GW emission following binary neutron star coalescence. In particular, we consider the development of analytic templates for the post-merger signal such as in [29] and their deployment using Bayesian inference algorithms such as those described in [66] of paramount importance and a high-priority goal for the follow-up of the imminent first detections of binary neutron star inspiral signals in the advanced detector era.

#### ACKNOWLEDGMENTS

The authors thank Francesco Pannarale for useful input and careful reading of this manuscript and S. Klimenko, I.S. Heng and M. West for helpful exchanges and discussion. J.C. and L.C. gratefully acknowledge support from NSF grant PHY-0955773. C.P. gratefully acknowledges NSF grants PHY-0970074, PHY-1307429 and the UWM Research Growth Initiative. A.B. is a Marie Curie Intra-European Fellow within the 7th European Community Framework Programme (IEF 331873). This work was supported by the Deutsche Forschungsgemeinschaft through Sonderforschungsbereich Transregio 7 “Gravitational Wave Astronomy”, and the Cluster of Excellence EXC 153 “Origin and Structure of the Universe”. Partial support comes from “NewCompStar”, COST Action MP1304. The computations were performed at the Rechenzentrum Garching of the Max-Planck-Gesellschaft, the Max Planck Institute for Astrophysics, and the Cyprus Institute under the LinkSCEEM/Cy-Tera project.

- 
- [1] G. M. Harry et al. (LIGO Scientific Collaboration), *Class. Quant. Grav.* **27**, 084006 (2010).
  - [2] T. Accadia et al., *Class. Quant. Grav.* **28**, 114002 (2011).
  - [3] T. V. Collaboration, Virgo Tech. Rep. VIR-027A-09 (2009), URL <https://tds.ego-gw.it/itf/tds/file.php?callFile=VIR-0027B-09Briggmann>
  - [4] K. Kuroda (LIGO Scientific Collaboration), *Class. Quant. Grav.* **27**, 084004 (2010).
  - [5] J. Aasi et al. (LIGO Scientific Collaboration and Virgo Collaboration), ArXiv e-prints (2013), 1304.0670.
  - [6] J. Abadie et al. (LIGO Scientific Collaboration and Virgo Collaboration), *Classical and Quantum Gravity* **27**, 173001 (2010), URL <http://stacks.iop.org/0264-9381/27/i=17/a=173001>.
  - [7] J. M. Lattimer and M. Prakash, *Physics Reports* **442**, 109 (2007), astro-ph/0612440.
  - [8] É. É. Flanagan and T. Hinderer, *Phys. Rev. D* **77**, 021502 (2008), 0709.1915.
  - [9] L. Baiotti, T. Damour, B. Giacomazzo, A. Nagar, and L. Rezzolla, *Phys. Rev. Lett.* **105**, 261101 (2010), 1009.0521.
  - [10] S. Bernuzzi, A. Nagar, M. Thierfelder, and X. Zhu, *Phys. Rev. D* **86**, 044030 (2012), 1205.3403.
  - [11] J. S. Read, C. Markakis, M. Shibata, K. Uryū, J. D. E. Creighton, and J. L. Friedman, *Phys. Rev. D* **79**, 124033 (2009), 0901.3258.
  - [12] X. Zhuge, J. M. Centrella, and S. L. W. McMillan, *Phys. Rev. D* **50**, 6247 (1994), gr-qc/9411029.
  - [13] M. Ruffert, H.-T. Janka, and G. Schaefer, *Astron. Astrophys.* **311**, 532 (1996), astro-ph/9509006.
  - [14] M. Shibata, *Phys. Rev. Lett.* **94**, 201101 (2005), gr-qc/0504082.

- [15] M. Shibata, K. Taniguchi, and K. Uryū, *Phys. Rev. D* **71**, 084021 (2005), gr-qc/0503119.
- [16] R. Oechslin, H.-T. Janka, and A. Marek, *Astron. Astrophys.* **467**, 395 (2007).
- [17] R. Oechslin and H.-T. Janka, *Phys. Rev. Lett.* **99**, 121102 (2007), astro-ph/0702228.
- [18] M. Anderson, E. W. Hirschmann, L. Lehner, S. L. Liebling, P. M. Motl, D. Neilsen, C. Palenzuela, and J. E. Tohline, *Phys. Rev. D* **77**, 024006 (2008), 0708.2720.
- [19] Y. T. Liu, S. L. Shapiro, Z. B. Etienne, and K. Taniguchi, *Phys. Rev. D* **78**, 024012 (2008), 0803.4193.
- [20] L. Baiotti, B. Giacomazzo, and L. Rezzolla, *Phys. Rev. D* **78**, 084033 (2008), URL <http://link.aps.org/doi/10.1103/PhysRevD.78.084033>.
- [21] K. Kiuchi, Y. Sekiguchi, M. Shibata, and K. Taniguchi, *Phys. Rev. D* **80**, 064037 (2009), 0904.4551.
- [22] N. Stergioulas, A. Bauswein, K. Zagkouris, and H.-T. Janka, *Mon. Not. Roy. Astron. Soc.* **418**, 427 (2011).
- [23] B. Giacomazzo, L. Rezzolla, and L. Baiotti, *Phys. Rev. D* **83**, 044014 (2011), 1009.2468.
- [24] K. Hotokezaka, K. Kyutoku, H. Okawa, M. Shibata, and K. Kiuchi, *Phys. Rev. D* **83**, 124008 (2011), 1105.4370.
- [25] Y. Sekiguchi, K. Kiuchi, K. Kyutoku, and M. Shibata, *prl* **107**, 051102 (2011), 1105.2125.
- [26] A. Bauswein and H.-T. Janka, *Physical Review Letters* **108**, 011101 (2012), 1106.1616.
- [27] A. Bauswein, H.-T. Janka, K. Hebeler, and A. Schwenk, *Phys. Rev. D* **86**, 063001 (2012).
- [28] A. Bauswein, T. W. Baumgarte, and H.-T. Janka, *Phys. Rev. Lett.* **111**, 131101 (2013).
- [29] K. Hotokezaka, K. Kiuchi, K. Kyutoku, T. Muranushi, Y. Sekiguchi, M. Shibata, and K. Taniguchi, *Phys. Rev. D* **88**, 044026 (2013).
- [30] S. Bernuzzi, T. Dietrich, W. Tichy, and B. Bruegmann, *ArXiv e-prints* (2013), 1311.4443.
- [31] K. Takami, L. Rezzolla, and L. Baiotti, *ArXiv e-prints* (2014), 1403.5672.
- [32] T. W. Baumgarte, S. L. Shapiro, and M. Shibata, *Astrophys. J. Lett.* **528**, L29 (2000), astro-ph/9910565.
- [33] A. Bauswein, N. Stergioulas, and H.-T. Janka, *ArXiv e-prints* (2014), 1403.5301.
- [34] M. Punturo, M. Abernathy, F. Acernese, B. Allen, N. Andersson, K. Arun, F. Barone, B. Barr, M. Barsuglia, M. Beker, et al., *Classical and Quantum Gravity* **27**, 084007 (2010).
- [35] C. Messenger, K. Takami, S. Gossan, L. Rezzolla, and B. S. Sathyaprakash, *ArXiv e-prints* (2013), 1312.1862.
- [36] B. F. Schutz, *Nature (London)* **323**, 310 (1986).
- [37] J. S. Read, L. Baiotti, J. D. E. Creighton, J. L. Friedman, B. Giacomazzo, K. Kyutoku, C. Markakis, L. Rezzolla, M. Shibata, and K. Taniguchi, *Phys. Rev. D* **88**, 044042 (2013), 1306.4065.
- [38] W. G. Anderson, P. R. Brady, J. D. Creighton, and É. É. Flanagan, *Phys. Rev. D* **63**, 042003 (2001), gr-qc/0008066.
- [39] S. Chatterji, L. Blackburn, G. Martin, and E. Katsavounidis, *Classical and Quantum Gravity* **21**, 1809 (2004), gr-qc/0412119.
- [40] S. Klimentenko and G. Mitselmakher, *Classical and Quantum Gravity* **21**, 1819 (2004).
- [41] P. J. Sutton, G. Jones, S. Chatterji, P. Kalmus, I. Leonor, S. Poprocki, J. Rollins, A. Searle, L. Stein, M. Tinto, et al., *New Journal of Physics* **12**, 053034 (2010), 0908.3665.
- [42] S. Klimentenko, S. Mohanty, M. Rakhmanov, and G. Mitselmakher, *Physical Review D* **72**, 122002 (2005).
- [43] S. Klimentenko, I. Yakushin, A. Mercer, and G. Mitselmakher, *Class. Quant. Grav.* **25**, 114029 (2008).
- [44] T. Z. Summerscales, A. Burrows, L. S. Finn, and C. D. Ott, *Astrophys. J.* **678**, 1142 (2008), 0704.2157.
- [45] C. Röver, M.-A. Bizouard, N. Christensen, H. Dimmelmeier, I. S. Heng, and R. Meyer, *Phys. Rev. D* **80**, 102004 (2009), 0909.1093.
- [46] J. Logue, C. D. Ott, I. S. Heng, P. Kalmus, and J. H. C. Scargill, *Phys. Rev. D* **86**, 044023 (2012), 1202.3256.
- [47] K. G. Arun, B. R. Iyer, B. S. Sathyaprakash, and P. A. Sundararajan, *Phys. Rev. D* **71**, 084008 (2005), gr-qc/0411146.
- [48] S. Fairhurst, *Classical and Quantum Gravity* **28**, 105021 (2011), 1010.6192.
- [49] J. Abadie et al. (LIGO Scientific Collaboration and Virgo Collaboration), *Phys. Rev. D* **85**, 122007 (2012), 1202.2788.
- [50] The LIGO Scientific Collaboration and the Virgo Collaboration: J. Abadie, et al., *Physical Review D* **85** (2012).
- [51] B. Allen, W. G. Anderson, P. R. Brady, D. A. Brown, and J. D. E. Creighton, *Phys. Rev. D* **85**, 122006 (2012), gr-qc/0509116.
- [52] J. Abadie et al. (LIGO Scientific Collaboration and Virgo Collaboration), *Phys. Rev. D* **85**, 082002 (2012), 1111.7314.
- [53] The LIGO Scientific Collaboration and the Virgo Collaboration: J. Aasi, et al., *Physical Review D* **87** (2013).
- [54] L. Blanchet, *Living Reviews in Relativity* **17** (2014), URL <http://www.livingreviews.org/lrr-2014-2>.
- [55] A. Buonanno, Y. Pan, J. G. Baker, J. Centrella, B. J. Kelly, S. T. McWilliams, and J. R. van Meter, *Phys. Rev. D* **76**, 104049 (2007), 0706.3732.
- [56] P. Ajith, M. Hannam, S. Husa, Y. Chen, B. Brügmann, N. Dorband, D. Müller, F. Ohme, D. Pollney, C. Reisswig, et al., *Physical Review Letters* **106**, 241101 (2011), 0909.2867.
- [57] F. Echeverria, *Phys. Rev. D* **40**, 3194 (1989).
- [58] P. Jaranowski, A. Królak, and B. F. Schutz, *Phys. Rev. D* **58**, 063001 (1998), gr-qc/9804014.
- [59] C. Pankow, S. Klimentenko, G. Mitselmakher, I. Yakushin, G. Vedovato, M. Drago, R. A. Mercer, and P. Ajith, *Classical and Quantum Gravity* **26**, 204004 (2009), 0905.3120.
- [60] B. P. Abbott et al. (LIGO Scientific Collaboration), *Phys. Rev. D* **80**, 102001 (2009), URL <http://link.aps.org/doi/10.1103/PhysRevD.80.102001>.
- [61] L. S. Finn and D. F. Chernoff, *Phys. Rev. D* **47**, 2198 (1993), gr-qc/9301003.
- [62] C. Cutler and É. E. Flanagan, *Phys. Rev. D* **49**, 2658 (1994), gr-qc/9402014.
- [63] P. Jaranowski, K. D. Kokkotas, A. Królak, and G. Tsegas, *Classical and Quantum Gravity* **13**, 1279 (1996).
- [64] J. Veitch, I. Mandel, B. Aylott, B. Farr, V. Raymond, C. Rodriguez, M. van der Sluys, V. Kalogera, and A. Vecchio, *Phys. Rev. D* **85**, 104045 (2012), 1201.1195.



- [65] M. Hannam, D. A. Brown, S. Fairhurst, C. L. Fryer, and I. W. Harry, *Astrophys. J. Lett.* **766**, L14 (2013), 1301.5616.
- [66] J. Aasi et al. (LIGO Scientific Collaboration and Virgo Collaboration), *Phys. Rev. D* **88**, 062001 (2013), 1304.1775.
- [67] G. Schwarz, *Annals of Statistics* **6**, 461 (1978).
- [68] J. Aasi et al. (The LIGO Scientific Collaboration, The Virgo Collaboration and The NINJA-2 Collaboration), *Class. Quant. Grav.* **31**, 115004 (2014), 1401.0939.
- [69] The LIGO Scientific Collaboration (2009), URL <https://dcc.ligo.org/LIGO-T0900288/public>.
- [70] T. Accadia et al. (2012), URL <https://tds.ego-gw.it/ql/?c=8940>.
- [71] B. P. Abbott et al. (The LIGO Scientific Collaboration), *Phys. Rev. D* **80**, 102002 (2009), URL <http://link.aps.org/doi/10.1103/PhysRevD.80.102002>.
- [72] J. Abadie et al. (The LIGO Scientific Collaboration and The Virgo Collaboration), *Phys. Rev. D* **81**, 102001 (2010), URL <http://link.aps.org/doi/10.1103/PhysRevD.81.102001>.
- [73] J. Isenberg and J. Nester, in *General Relativity and Gravitation* (Plenum Press, New York, 1980), p. 23.
- [74] J. R. Wilson, G. J. Mathews, and P. Marronetti, *Phys. Rev. D* **54**, 1317 (1996).
- [75] R. Oechslin, S. Rosswog, and F.-K. Thielemann, *Phys. Rev. D* **65**, 103005 (2002).
- [76] A. Bauswein, H.-T. Janka, and R. Oechslin, *Phys. Rev. D* **82**, 084043 (2010).
- [77] D. S. Balsara, *Journal of Computational Physics* **121**, 357 (1995).
- [78] J. M. Lattimer, *Annu. Rev. Nucl. Part. Sci.* **62**, 485 (2012).
- [79] P. B. Demorest, T. Pennucci, S. M. Ransom, M. S. E. Roberts, and J. W. T. Hessels, *Nature (London)* **467**, 1081 (2010).
- [80] J. Antoniadis, P. C. C. Freire, N. Wex, T. M. Tauris, R. S. Lynch, M. H. van Kerkwijk, M. Kramer, C. Bassa, V. S. Dhillon, T. Driebe, et al., *Science* **340** (2013).
- [81] A. Akmal, V. R. Pandharipande, and D. G. Ravenhall, *Phys. Rev. C* **58**, 1804 (1998), nucl-th/9804027.
- [82] G. A. Lalazissis, J. König, and P. Ring, *Phys. Rev. C* **55**, 540 (1997).
- [83] M. Hempel and J. Schaffner-Bielich, *Nucl. Phys. A* **837**, 210 (2010).
- [84] S. Typel, G. Röpke, T. Klähn, D. Blaschke, and H. H. Wolter, *Phys. Rev. C* **81**, 015803 (2010).
- [85] H. Shen, H. Toki, K. Oyamatsu, and K. Sumiyoshi, *Nucl. Phys. A* **637**, 435 (1998).
- [86] Y. Sugahara and H. Toki, *Nuclear Physics A* **579**, 557 (1994).
- [87] M. Hempel, T. Fischer, J. Schaffner-Bielich, and M. Liebendörfer, *Astrophys. J.* **748**, 70 (2012).
- [88] A. W. Steiner, M. Hempel, and T. Fischer, *Astrophys. J.* **774**, 17 (2013), 1207.2184.
- [89] H. Toki, D. Hirata, Y. Sugahara, K. Sumiyoshi, and I. Tanihata, *Nuclear Physics A* **588**, 357 (1995).
- [90] L. Bildsten and C. Cutler, *Astrophys. J.* **400**, 175 (1992).
- [91] C. S. Kochanek, *Astrophys. J.* **398**, 234 (1992).
- [92] M. Dominik, K. Belczynski, C. Fryer, D. E. Holz, E. Berti, T. Bulik, I. Mandel, and R. O'Shaughnessy, *Astrophys. J.* **759**, 52 (2012).
- [93] A. Bauswein, H.-T. Janka, K. Hebeler, and A. Schwenk, *Phys. Rev. D* **86**, 063001 (2012), 1204.1888.
- [94] M. Shibata and K. Taniguchi, *Phys. Rev. D* **73**, 064027 (2006), astro-ph/0603145.
- [95] S. L. Shapiro, *Astrophys. J.* **544**, 397 (2000), astro-ph/0010493.
- [96] V. Paschalidis, Z. B. Etienne, and S. L. Shapiro, *Phys. Rev. D* **86**, 064032 (2012), 1208.5487.
- [97] A. Reisenegger and A. Bonacic, in *Pulsars, AXPs and SGRs Observed with BeppoSAX and Other Observatories*, edited by G. Cusumano, E. Massaro, and T. Mineo (2003), pp. 231–236, astro-ph/0303454.
- [98] N. Andersson and K. D. Kokkotas, *Mon. Not. Roy. Astron. Soc.* **299**, 1059 (1998), gr-qc/9711088.
- [99] John L. Friedman and Nikolaos Stergioulas, *Rotating Relativistic Stars* (Cambridge University Press, 2013).
- [100] E. Gaertig and K. D. Kokkotas, *Phys. Rev. D* **83**, 064031 (2011), 1005.5228.
- [101] D. D. Doneva, E. Gaertig, K. D. Kokkotas, and C. Krüger, *Phys. Rev. D* **88**, 044052 (2013), 1305.7197.
- [102] B. Zink, O. Korobkin, E. Schnetter, and N. Stergioulas, *Phys. Rev. D* **81**, 084055 (2010), 1003.0779.
- [103] C. Krüger, E. Gaertig, and K. D. Kokkotas, *Phys. Rev. D* **81**, 084019 (2010), 0911.2764.
- [104] G. F. Burgio, V. Ferrari, L. Gualtieri, and H.-J. Schulze, *Phys. Rev. D* **84**, 044017 (2011), 1106.2736.
- [105] P. Jaranowski and A. Krlak, *Living Reviews in Relativity* **15** (2012), URL <http://www.livingreviews.org/lrr-2012-4>.
- [106] P. J. Sutton, ArXiv e-prints (2013), 1304.0210.
- [107] T. B. Littenberg and N. J. Cornish, *Phys. Rev. D* **82**, 103007 (2010), 1008.1577.
- [108] N. J. Cornish, ArXiv e-prints (2012), 1204.2000.